Single-Particle Configurations in the Neutron-Deficient Nuclides ^{158}W and ^{152}Yb

Thesis submitted in accordance with the requirements

of the University of Liverpool

for the degree of Doctor of Philosophy

by

Liliana Donosa

Oliver Lodge Laboratory

2014

Contents

List of Figures

List of Tables

ABSTRACT

Excited states in the highly neutron-deficient nuclei ^{158}W and ^{152}Yb have been observed for the first time in recoil-decay tagging experiments at the University of Jyväskylä Accelerator Laboratory using the JUROGAM and GREAT spectrometers in conjunction with the RITU gas-filled separator.

The level scheme in ^{158}W has been established for the first time in a recoil-decay tagged $\gamma\gamma$-coincidence analysis. The ground state band is established up to $I^{\pi} = 6^{+}$, which is the maximum spin permitted for a seniority $\nu = 2 \, \nu f_{7/2}^{2}$ configuration. Excited states have also been established on the alpha-decaying 8^{+} isomer and interpreted in terms of $\nu = 4$ configurations.

The previous studies of the ^{152}Yb (N = 82) have identified isomeric states corresponding to $J^{\pi} = 10^{+}$. These states are thought to be based on two fully aligned $h_{11/2}$ protons possessing seniority $\nu = 2$. The excited states above isomeric 10^{+} states were for established for the first time by successive breaking and aligning of the $\pi h_{11/2}$ having $\nu = 4$ seniority.

Chapter 1

Introduction

There is a great contemporary interest in studying the structure of heavy nuclei close to both closed shells and the proton drip line. This thesis focuses on the highly neutron-deficient nuclei ^{158}W and ^{152}Yb, which are near/at the $N = 82$ shell closure and between the established proton shell closures at $64 \leq Z \leq 82$. Figure 1.1 highlights the location of these nuclides and their mass region. Experimental investigations of excited states in heavy nuclei provide an important means of testing and constraining the nuclear shell model yet very little is known about the excited states of such heavy exotic species. Nuclei in the vicinity of the shell closures at $Z = 64$, $Z = 82$ and $N = 82$ provide an excellent laboratory for testing the role of a small number of specific single-particle orbitals in generating angular momentum and for determining the relative positions of these orbitals.

Experimental studies are challenging in this mass region. The fusion evaporation reactions that are used to populate nuclei in this mass region often have a large number
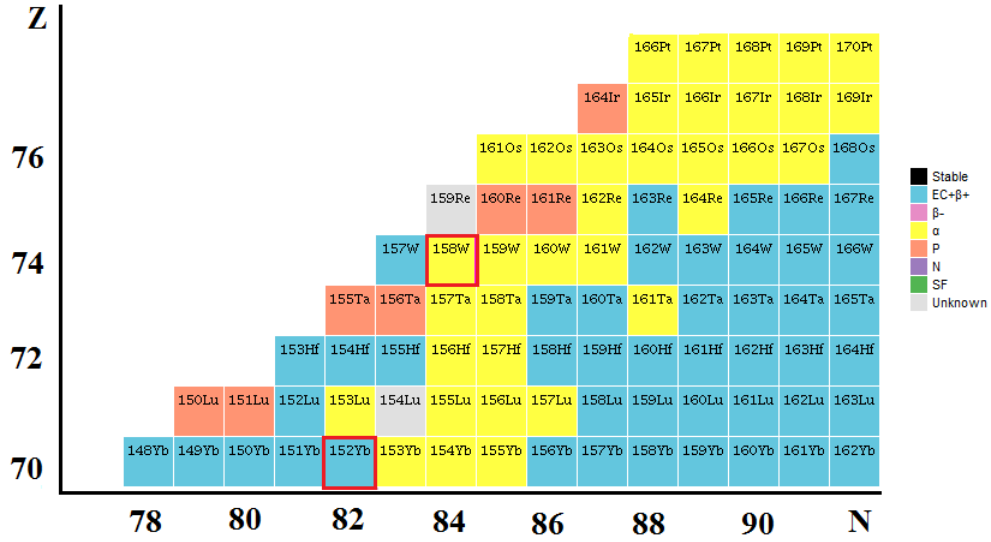
Figure 1.1: The chart of nuclides show the region of interest. The nuclei detailed in this work are highlighted in red squares [1].

of open exit channels. Typically the reaction channels of interest have a relatively low production cross section compared with other fusion channels, which in turn are much lower than the fission process that often dominates the total reaction cross section. Consequently, the γ-ray cascades that provide information on the structure of excited states in these exotic nuclei are almost entirely obscured.

However, the application of selective experimental methods such as the recoil-decay tagging technique, used in conjunction with dedicated apparatus, helps to suppress these huge backgrounds and identify new structures.

The experiments discussed in this thesis were performed at the University of Jyväskylä Accelerator Laboratory [2] using the JUROGAM γ-ray spectrometer in conjunction with the RITU gas-filled separator and the GREAT focal plane spectrometer.

2

In this work it has been possible to identify an excitation level scheme in ^{158}W $N = 84$ for the first time and investigate the role of neutron excitations involving the $\nu f_{7/2}$ and $\nu h_{9/2}$ orbitals. Excited states have also been established for the first time above the 10^+ microsecond isomer in ^{152}Yb, which is the heaviest even-Z isotone studied to high spin. The closed neutron shell at $N = 82$ is robust to excitations at low energy and high spin states are expected to be generated by aligning the spins of valence protons in the $h_{11/2}$ subshell. Both nuclei are compared with shell model calculations.

The second chapter discusses the relevant nuclear structure theory including the shell model and potentials. The third chapter is describing the experimental set-ups at the University of Jyväskylä including the HPGe detectors for detection of prompt γ-rays at the target position, the RITU separator and the GREAT spectrometer. Chapters 4 and 5 present self-contained chapters detailing the analysis, results and interpretations of the excited states in ^{158}W and ^{152}Yb.

Chapter 2

Theoretical Background

2.1 The Shell Model

It is currently an intractable problem to predict the observable properties of heavy nuclei from the large number of mutual interactions between the constituent nucleons. It is necessary to make approximations assuming a mean field with an effective interaction. The shell model was devised in the 1940s by Mayer and Jensen who proposed the model as a solution for explaining experimental observations at certain nucleon numbers. The spherical shell model is a simple model applying the approximation that the nucleons in the nucleus move in a potential $U(i)$ generated by the mutual interactions of all the other nucleons. The many-body problem is reduced to a simple case of a single particle moving in a mean-field potential taking into consideration only the spin, charge coordinates, effective residual interaction so the problem is limited to the first order or at most second order perturbation theory.
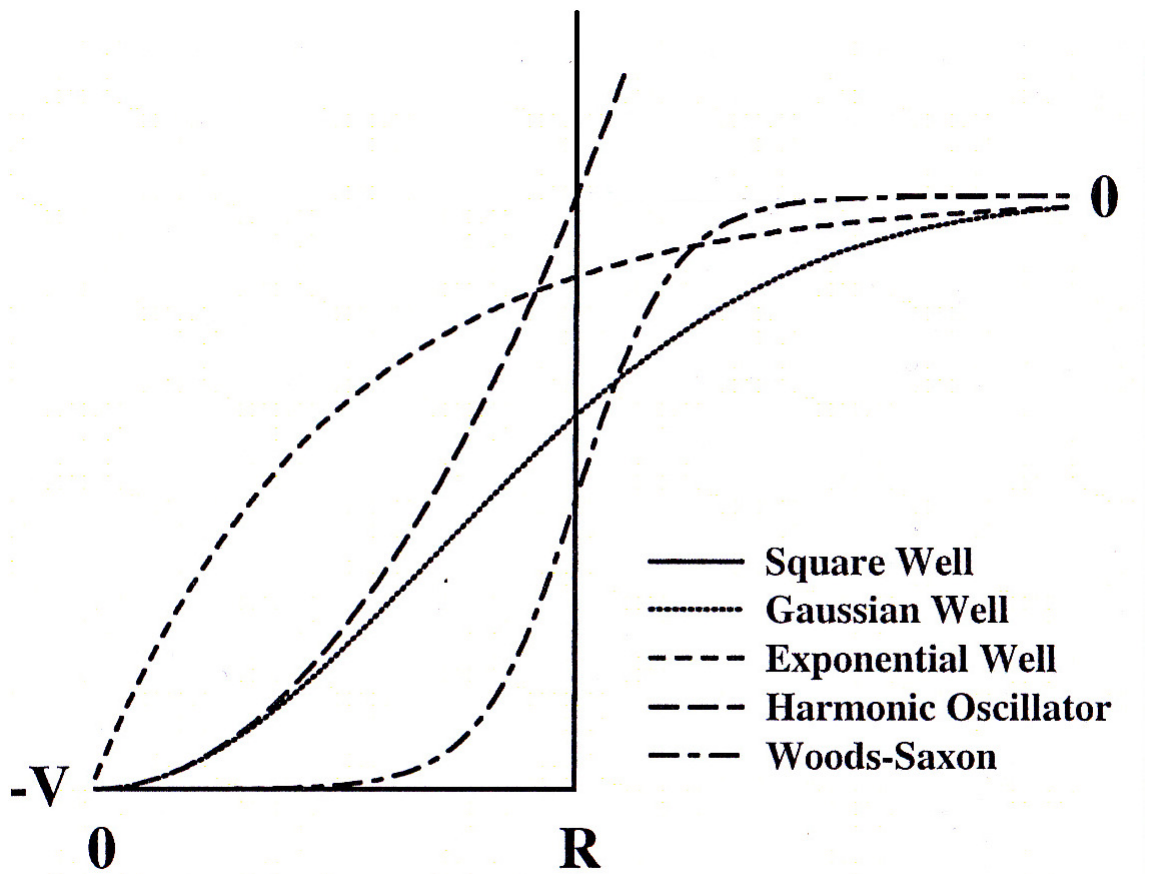
Figure 2.1: A comparison of some of the potential wells used in describing the nuclear potential. Picture taken from [3].

The success of the model depends largely in describing the shape of the average mean-field potential. Many potentials have been considered such as the Harmonic Oscillator, Square Well and Woods-Saxon. Some potentials are more realistic approximations than others. For example, the harmonic oscillator potential, while being easy to use from an analytical perspective, is unrealistic since it requires an infinite energy to separate protons or neutrons, see Fig. 2.1. A more realistic potential is the

Woods-Saxon potential, which accounts for the diffuseness of the nuclear surface and the flatness of the potential for the most bound nucleons and is defined as

$$V(r) = \frac{-V_0}{1 + exp[(r - R)/a]},$$ (2.1)

where V_0 is the depth of the well of order 50 MeV, a = 0.524 fm is the skin thickness and R = $1.25A^{1/3}$ is the radius.

A simple potential can generate experimental features such as the *magic numbers*. The shell model diagram calculated with a harmonic oscillator potential yields magic numbers at 2, 8, 20, 40, 70, 112, 168 as is represented in Fig. 2.2. A spin-orbit ($l \cdot s$) interaction was introduced by Mayer in the 1940s ([5]). The effect of this interaction is to relieve the degeneracy of the oscillator states. The total angular momentum of a nucleon is $j = l + s$, where l is the orbital angular quantum number and s is the spin of the nucleon which is $\pm 1/2$. Nuclear subshells for a given l value are represented by the spectroscopic notation represented in the Table 2.1.

Table 2.1: Spectroscopic notations for l values.

l	0	1	2	3	4	5	6
Symbol	s	p	d	f	g	h	i

The possible values of the total angular momentum are $j = l + 1/2$ or $j = l - 1/2$. The total angular momentum of a nucleus with A nucleons is the vector sum of all nucleons. The degeneracy of each level is (2j+1). The energy splitting is proportional
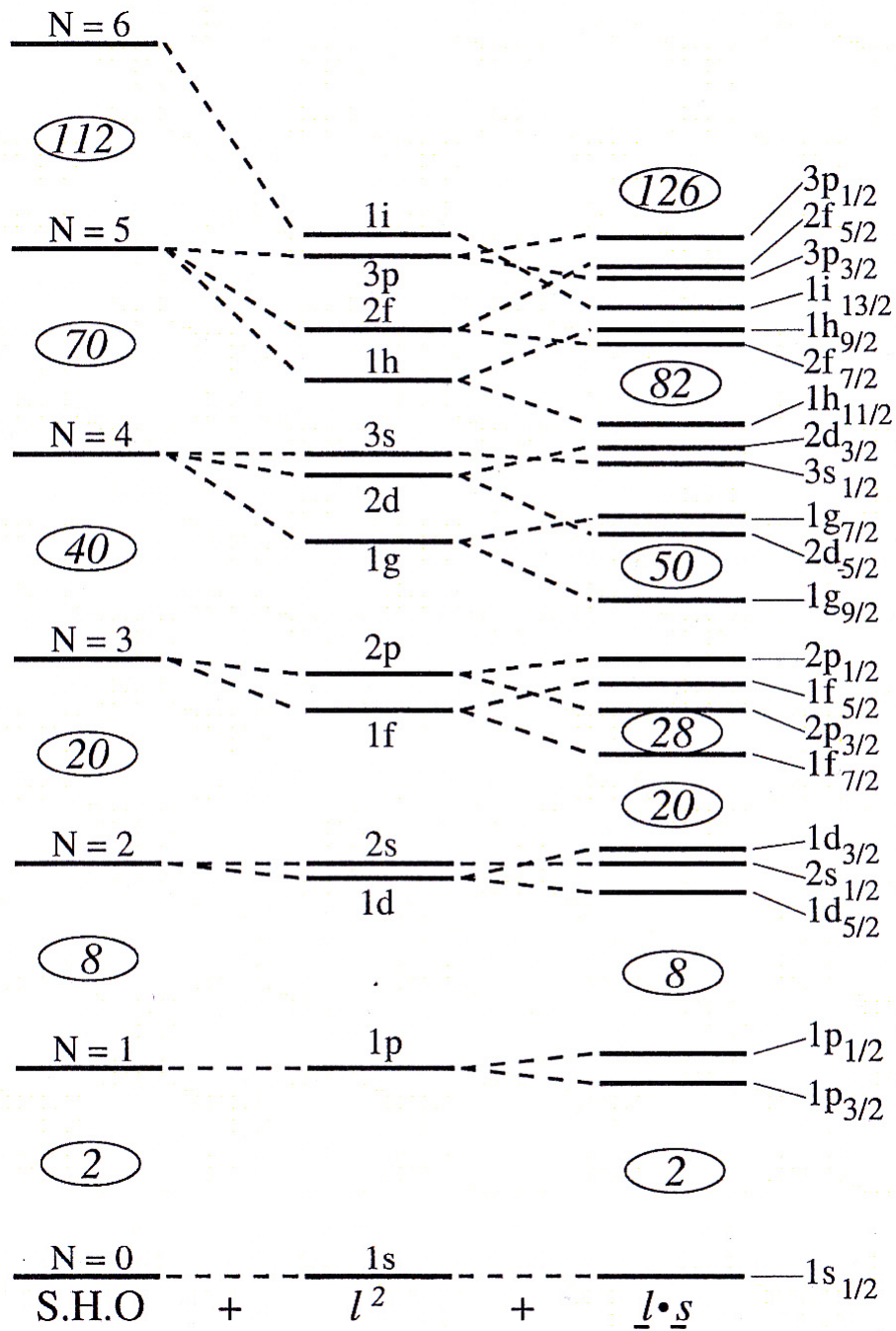
Figure 2.2: Magic numbers obtained from the Harmonic Oscillator potential including the spin-orbit interaction [4].

to l [6] and gives rise to the correct magic numbers. The magic numbers appear when gaps form between the intruder states with higher total angular momentum $j = l + 1/2$ that are more tightly bound and the natural parity states. For example, the $1f_{7/2}$ orbit is introduced between the $1d_{3/2}$ and $2p_{3/2}$ orbits resulting in the magic number 28. By including the spin-orbit interaction the magic numbers produced are: 2, 8, 20, 50, 82, 126 and 184 (Fig. 2.2).

2.2   Radioactive Decay

2.2.1   Alpha Decay

Heavy radioactive nuclei have the tendency to spontaneously emit nucleons and change into another more stable nucleus with a higher binding energy per nucleon. The main decay processes by which heavy nuclei can increase their binding energy per nucleon are alpha decay and nuclear fission.

In alpha decay, the heavy nucleus expels a helium nucleus. Nuclei which emit an α particle form a decay chain of nuclei whose mass decreases by 4 mass units until either a stable nucleus is reached or another decay process predominates. In the fission process the nucleus will break into two lower mass nuclei. In both processes binding energy will be transferred into the kinetic energy of the reaction products.

2.2.2 α decay equation

The process of α decay can be represented as follows
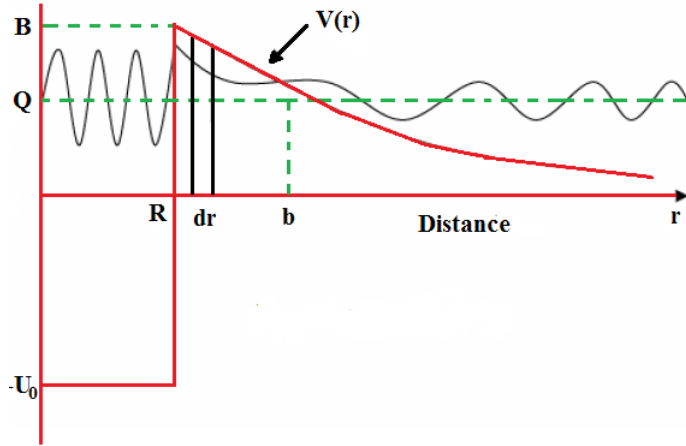
Figure 2.3: The alpha-decay potential. The height of the potential is defined by the Coulomb potential and b is the turning point.

$$^A_Z X_N \rightarrow ^{A-4}_{Z-2} X_{N-2} + \alpha, \tag{2.2}$$

where α is a ^4He nucleus with two protons and two neutrons.

Neglecting the electron binding energy difference and assuming the initial nucleus to be at rest, the conservation of the mass-energy requires the final energy to be divided between the masses of the nuclei as

$$Q_\alpha = (M_A - M_{A-4} - M_\alpha)c^2. \tag{2.3}$$

Nuclear mass measurements denote that the nuclei unstable toward α emission occurs at A $\approx$ 150. The disintegration energy Q_α must be 4 MeV for alpha decay to occur [6, 7]. It is also observed that nuclei with large Q have shorter half life (s) $T_{1/2} = \frac{ln2}{\lambda_\alpha}$. The disintegration energy decreases with addition of neutrons, increasing the half-life.

2.2.3 Theory of α decay emission

The process of α decay can be considered as an initial bound system comprising a preformed α-particle bound to the daughter nucleus, which undergoes three phases of interaction with the potential. A schematic diagram of the potential is presented in Fig.2.3.

The first region is where the α particle is inside the nucleus at $r \leq R$ and cannot escape. The second region around the potential barrier is produced at $R \leq r \leq b$. The α particle is outside the nucleus when $r > b$ where b is the turning point. From the classical point of view, the α particle cannot escape from the barrier. Gamow and Gurney conceived a theory in 1928 to explain the α emission i.e. it was possible to discuss the α particle tunnelling through barrier [6]. In the quantum mechanics case, it is assumed the Coulomb barrier is made of a series of square barriers of width dr. The Coulomb barrier for α particle of a charge ze and the daughter nucleus of a charge $Z'e = (Z - z)e$ outside the nucleus is

$$V_C = \frac{zZ'e^2}{4\pi\varepsilon_0 r}. \tag{2.4}$$

The probability to penetrate one of the barriers is e^{-2Kdr} where the wave function of each barrier is given by

$$K = \sqrt{2M_\alpha(\frac{zZ'e^2}{4\pi\varepsilon_0 r} - Q_\alpha)/\hbar^2}. \tag{2.5}$$

Then, the total penetration probability [8] is expressed as

$$P = exp(-2\int_R^b K dr) = e^{-G}, \tag{2.6}$$

where G is the *Gamow factor* given by the formula

$$G = \frac{2}{\hbar} \int_R^b \sqrt{2M_\alpha(V(r) - Q_\alpha)} dr. \tag{2.7}$$

Larger disintegration energy results in a thinner barrier, a higher penetration probability and a shorter half-life [6, 9].

The α decay rate can be calculated as follows

$$\lambda_\alpha = fP = fe^{-G}, \tag{2.8}$$

where f is the frequency of the particle at the barrier $\approx 10^{21}$ (s^{-1}).

The formula for the half-life is

$$t_{1/2} = \frac{ln2}{\lambda_\alpha}. \tag{2.9}$$

In describing the decay process it was assumed that the α particle pre-exists within the nucleus with zero angular momentum. The case becomes more complicated to solve the situation if $l \neq 0$ and a centrifugal barrier must be added to Coulomb barrier.

2.3   Electromagnetic decay modes

2.3.1   Gamma-Ray Selection Rule

Gamma-ray emission is the decay from an initial state of I_i^π to a final state of I_f^π via electromagnetic radiation. Conservation laws play an important role dictating the properties of the γ ray. Photons carry an intrinsic spin $1\hbar$ and an angular momentum l. The total angular momentum of the γ ray is $L = l + s$.

11

The conservation of angular momentum and parity lead to the following *selection rules* [6] as

$$|I_i - I_f| \leq L \leq |I_i + I_f|. \tag{2.10}$$

The parity of γ-ray emitted in a magnetic transition carrying an angular momentum L is

$$\pi(M) = \pi_i \pi_f = (-1)^{L+1}, \tag{2.11}$$

and for an electric transition is given by

$$\pi(E) = \pi_i \pi_f = (-1)^L. \tag{2.12}$$

The parity is utilised to determine the multipolarity of the radiation . If there is no change in parity the radiation field has even parity, while if there is a change in parity the radiation field has odd parity (Table 2.2).

Table 2.2: Selection rule for gamma-ray transitions.

δ I $= \mid$ I$_i$ - I$_f$ $\mid$	1	2	3	4	5
Parity change	E1	M2	E3	M4	E5
No parity change	M1	E2	M3	E4	M5

The γ-ray transition probability [10, 11] for a state decaying from the initial state I$_i$ to a final state I$_f$ is

$$\lambda_{i \to f}^{ML,EL} = \frac{8\pi(L+1)}{\hbar L[(2L+1)!!]^2}(\frac{\omega}{c})^{2L+1}B(\begin{smallmatrix}M\\\\E\end{smallmatrix}, L, I_i \to I_f), \tag{2.13}$$

$$B(\begin{smallmatrix}M\\\\E\end{smallmatrix}, L, I_i \to I_f) = \frac{1}{2I_i + 1}|\langle I_f\| \begin{smallmatrix}\mathcal{M}(M_L)\\\\\mathcal{M}(E_L)\end{smallmatrix} \|I_i\rangle|^2, \tag{2.14}$$

where B($\begin{smallmatrix}M\\\\E\end{smallmatrix}$, L, I$_i$ → I$_f$) is the reduced matrix element, $\mathcal{M}(M_L)$ and $\mathcal{M}(E_L)$ are the magnetic and electric multipole operators.

The transition probability for a mixed multipole (es E$_2$/M$_1$), is calculated with multipole mixing ratio δ [12] as

$$\delta = \frac{\langle\|L+1\|\rangle}{\langle\|L\|\rangle}, \tag{2.15}$$

$$\delta^2 = \frac{intensity(L+1)}{intensity(L)}. \tag{2.16}$$

The multipolarity calculations give information about change in spin and parity between the nuclear states. Transitions are classified as electric or magnetic based on whether the radiation is due to charge or current distribution.

The transition probability λ (s^{-1}) is linked to the lifetime τ of the decaying excited state connected to its intrinsic width (Γ) given by Heisenberg's uncertainty principle as

$$\tau\Gamma \approx \hbar. \tag{2.17}$$

The lifetime of the energy levels can be estimated for any multipolarity with Weisskopf estimates. The Weisskopf estimates estimates the reduced matrix element

based on the single particle spherical shell model. The reduced matrix element is presented below

$$\left| \langle I_f \| \begin{array}{c} \mathcal{M}(M_L) \\ \mathcal{M}(E_L) \end{array} \| I_i \rangle \right|^2. \tag{2.18}$$

The model assumes, for an electric single-particle transition, the excitation of only one nucleon in the potential that changes its orbit without affecting the rest of the nucleons in the nucleus. In the case of a magnetic transition the intrinsic spin is flipped i.e. $j_i = l_i \pm 1/2 \rightarrow j_i = l_i \mp 1/2$. The reduced matrix element and the transition probabilities of electric and magnetic transition with Weisskopf estimates are

$$B(EL) = 4.4 \times 10^{21} \frac{(L+1)}{L[(2L+1)!!]^2} \left(\frac{3}{L+3}\right)^2 \frac{r_0^{2L}}{(\hbar c)^{2L+1}} A^{\frac{2L}{3}} E_\gamma^{2L+1}, \tag{2.19}$$

$$\lambda^{EL} \approx \frac{2(L+1)}{L[(2L+1)!!]^2} \left(\frac{3}{L+3}\right)^2 \left(\frac{e^2}{\hbar c}\right) \omega (kR)^{2L}, \tag{2.20}$$

$$B(ML) = 1.32 \times 10^{21} \frac{(L+1)}{L[(2L+1)!!]^2} \left(\frac{3}{L+2}\right)^2 \frac{r_0^{(2L-2)}}{(\hbar c)^{2L+1}} A^{\frac{2L-2}{3}} E_\gamma^{2L+1}, \tag{2.21}$$

$$\lambda^{ML} \approx 10 \frac{2(L+1)}{L[(2L+1)!!]^2} \left(\frac{3}{L+2}\right)^2 \left(\frac{e^2}{\hbar c}\right) \left(\frac{\hbar c}{mc^2 R}\right)^2 \omega (kR)^{2L}. \tag{2.22}$$

In Table 2.3 are estimates for some of the lower multipole order.

When the Weisskopf estimates are similar to measured values it suggests that a single particle change has occurred. A high difference between the Weisskopf estimates and the true value suggests a collective nature.

$B(E1) = 1.0 \times 10^{14} A^{2/3} E_\gamma^3$	$B(M1) = 3.1 \times 10^{13} E_\gamma^3$
$B(E2) = 7.3 \times 10^7 A^{4/3} E_\gamma^5$	$B(M2) = 2.2 \times 10^7 A^{2/3} E_\gamma^5$
$B(E3) = 34 A^2 E_\gamma^7$	$B(M3) = 10 A^{4/3} E_\gamma^7$
$B(E4) = 1.1 \times 10^{-5} A^{8/3} E_\gamma^9$	$B(M4) = 3.3 \times 10^{-6} A^2 E_\gamma^9$

2.3.2 Internal Conversion

Gamma-ray emission occurs when changes in the nuclear structure give rise to changes in the surrounding electromagnetic field. The nucleus can also interact with innermost electrons of the atom through electromagnetic forces. In internal conversion energy is transferred to the electron, and if this energy exceeds the binding energy of the atomic electrons, it will emitted with a kinetic energy given by formula

$$E_{e^-} = E_\gamma - BE_{electron}, \tag{2.23}$$

where E_γ is the energy of the γ decay and $BE_{electron}$ is the electron binding energy.

This process is called *internal conversion*. In the atom will be a vacancy which will be filled by another electron from higher shell with emission of X ray used to identify the proton number of the nucleus of interest. The electrons emitted are from different atomic shells most likely from the inner shell electrons (K,L,M...), because of that the electrons come out with different energies.

The total transition probability [10] is given by

$$\lambda_t = \lambda_\gamma + \Sigma\lambda_i = \lambda_\gamma(1 + \Sigma\alpha_i), \tag{2.24}$$

where the λ_i is the i-shell electron conversion probability and α_i is the i-shell internal conversion coefficient.

The conversion electron depends on the multipolarity, giving information about spin and parity of transitions between nuclear states, measured from the internal conversion coefficient $\alpha = \frac{\lambda_e}{\lambda_\gamma}$ [6, 10] or ratio of the partial conversion coefficient $\frac{\alpha_M}{\alpha_L}$. The conversion coefficients for electric and magnetic multipoles [6] are calculated with following formula

$$\alpha(E) = \frac{Z^3}{n^3}\left(\frac{L}{L+1}\right)\left(\frac{e^2}{4\pi\epsilon_0\hbar c}\right)^4\left(\frac{2m_ec^2}{E}\right)^{L+5/2}, \tag{2.25}$$

$$\alpha(M) = \frac{Z^3}{n^3}\left(\frac{e^2}{4\pi\epsilon_0\hbar c}\right)^4\left(\frac{2m_ec^2}{E}\right)^{L+3/2}, \tag{2.26}$$

where n is the principal quantum number of the bound electron wave function, Z is the atomic number and the ($e^2/4\,\pi\,\epsilon_0\,\hbar$ c) is the fine structure constant ~ 0.0073. This is a non-relativistic calculation illustrating a number of features of the internal conversion coefficient, such as:

• an increase with increasing atomic number of the nucleus.

• an increase with multipolarity.

• a decrease with increasing transition energy.

2.3.3 Isomers

Isomers decay to lower energy states sometimes to ground state of the nuclide through γ emission or particle emission. Nuclear isomers have half-lives at least 100 times more than typical gamma decay times ($\sim 10^{-12}s$). Long-lived isomers are interesting because they give information about the properties of the state such as spin and multipolarity of the decaying transition as well as giving an understanding of the single-particle structure of the isomeric state and the neighbouring excited states. The *island of isomerism* is noticed at nuclei closed by the magic numbers 50, 82 or 126. In general there are four types of isomers which are listed below.

2.3.4 Spin Isomers

Spin trap isomers were discovered in spherical nuclei or near spherical nuclei. Decay from excited states by γ-ray emission or internal conversion required a high change in spin and the radiation is emitted with a high multipolarity which incurs a longer lifetime [13].

2.3.5 Seniority Isomers

Seniority was introduced by Racah in atomic physics and applied later in nuclear structure referring to the number of nucleons that are not in pairs coupled to angular momentum $J^{\pi} = 0^{+}$. The seniority scheme is found particularly in semi-closed nuclei where states with low seniority occur at low energy. The case of ^{152}Yb studied in this thesis, presents a case of a semi-closed nucleus where only the proton excitations of

the valence nucleons (6 in total) generate the excited states. In the ground state all the nucleons are paired in the even-even nucleus ^{152}Yb giving the seniority 0. The isomeric 10^+ state is formed by the coupling of two protons in $h_{11/2}$ of seniority 2. To make states of higher spin it is necessary to break a pair of nucleons. The maximum spin produced for the semi-closed nucleus is $J^\pi = 16^+$ with a seniority $\nu = 4$.

2.3.6 K-Isomers

K-isomers occur when there are large changes in the spin orientation relative to the axis of symmetry. K is the projection of total angular momentum of a nucleon state on the symmetry axis and can be used to label nuclear states [14]. This type of isomer is seen most often in prolate deformed nuclei where the long axis is the axis of symmetry. Electromagnetic transitions from a state K_i to a state K_f change K by $\Delta K = K_i - K_f$. Electromagnetic transitions of multipolarity λ are forbidden if $K > \lambda$. K-forbidden transitions violate the usual K-selection rules i.e. a nucleus changes from having its angular momentum generated by individual nucleons rotating around the symmetry axis (large K) to collective rotation perpendicular to the symmetry axis (small K).

2.3.7 Shape Isomers

Shape isomers occur where the potential energy has one or more additional minima over and above the ground-state minimum. When an additional minima is sufficiently deep, then the nucleus may exist in a state corresponding to the energy and shape of this minimum; this state is a shape isomer. An example of the shape isomers are

the fission isomers in heavy nuclei [14]. The life time of these isomers depends on the overlap of the wave function of the shape isomers and the ground state.

Chapter 3

Experimental Methodology

Obtaining information on nuclear structure of exotic nuclei is challenging without the application of selective techniques using dedicated apparatus. The apparatus used to perform γ-ray spectroscopy approaching the proton drip line will be discussed in this chapter. The prompt γ-rays are detected at the target position with HPGe detectors. The separation of the recoils from the unreacted beam is possible with a recoil ion transport unit separator followed at the focal plane by a combination of detectors for detection of delayed γ rays, α particles, recoiling nuclei and conversion electrons. The mechanisms for synthesizing exotic nuclei will also be discussed.

The fusion-evaporation reactions utilised in this work produce many open exit channels and generate a large γ-ray background. The Recoil Decay Tagging (RDT) method is utilized to make a good correlation of the recoiling nucleus with its subsequent decay at the focal plane and correlated with γ rays at the target plane. The delayed γ rays above isomeric state were obtained by applying the recoil isomeric tagging

(RIT) method. The data, time stamped with a precision of 10 ns and synchronised, is collected and analysed off-line by the GRAIN [15] analysis software package.

3.1 Synthesis of Exotic Nuclei

Fusion evaporation reactions take place when a projectile and a target fuse together to form a compound nucleus (CN). In this process the CN receives an amount of angular momentum given by $b \times p$ where b is the impact parameter and p is the linear momentum of the beam. The kinetic energy of the beam should be sufficient to overcome the Coulomb barrier defined by

$$V_{CB} = \frac{e^2}{4\pi\epsilon_0} \frac{Z_B Z_T}{R_B + R_T},$$

(3.1)

where Z_B, Z_T are the atomic numbers of the projectile and the target, while R_B, R_T are the radii of the projectile and the target. In Fig. 3.1 are represented the stages of the fusion evaporation process.

The second stage of the fusion evaporation reaction is when the compound nucleus starts to lose energy by evaporating nucleons (protons, neutrons and α). The excitation energy of the compound nucleus decreases by 5-8 MeV with every particle emitted as well as removing 1-2 $\hbar$ of the angular momentum. The compound nucleus takes 10^{-15} s to decay into a residual nucleus which is neutron deficient. The residual nucleus is left in an excited state and decays to the ground state after 10^{-9}s by the emission of γ rays with low multipolarities (and/or conversion electrons) along the yrast line.

21
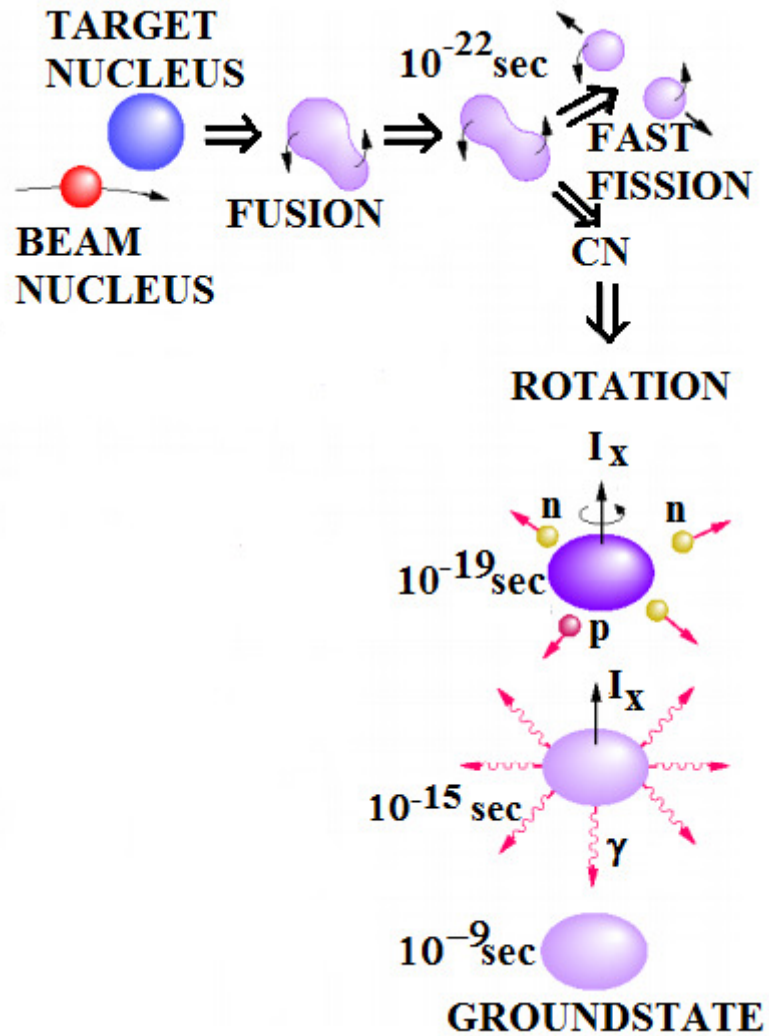
Figure 3.1: The key stages of a fusion evaporation reaction when a ^{58}Ni projectile fuses with a ^{102}Pd target and a compound nucleus is formed. The compound nucleus in a highly excited state initially cools down by evaporating nucleons. The residual nucleus, being in an excited state decays to the ground state by emitting γ rays [3].

The yrast states have the lowest excitation energy for a given value of angular momentum (Fig. 3.2). The particle evaporation occurs until the excitation of the
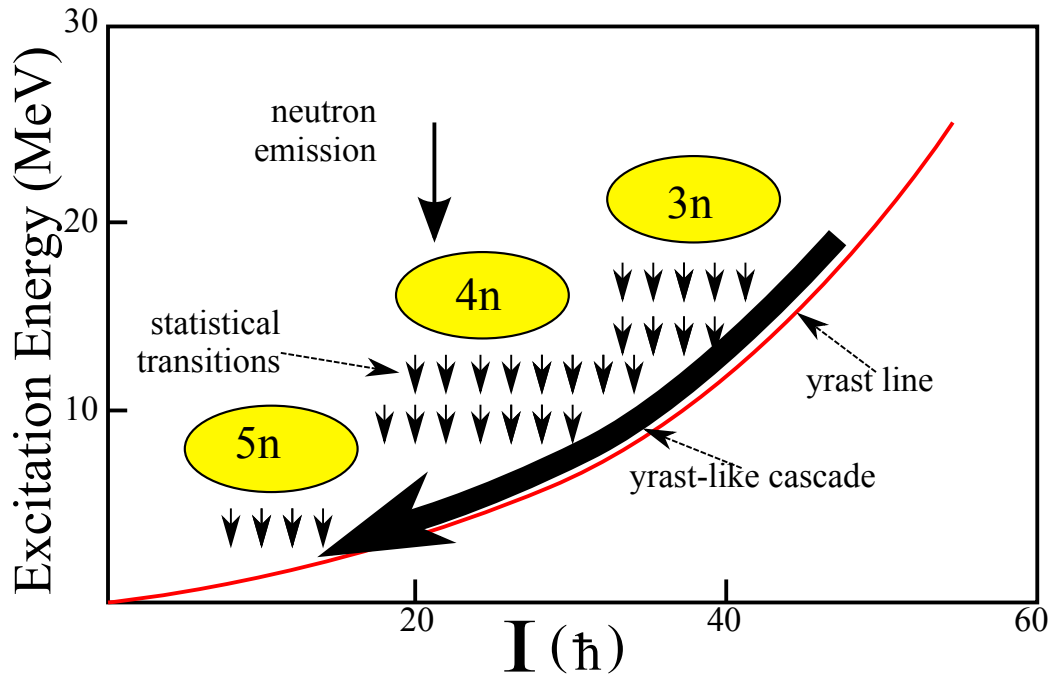
Figure 3.2: A figure of the E-I plane representing the de-excitation of a compound nucleus. The yrast line is highlighted.

compound nucleus is ~ 8 MeV above the yrast line. Evaporation of particles can typically leave the nucleus in states with high excitation energy and angular momentum ($I_c < 70\hbar$).

3.1.1 Angular Distribution

In a reaction, such as the fusion evaporation reaction discussed in this chapter, a lot of nuclei were produced. Information about spins of the excited states of the nucleus under study are determined by applying the angular distribution measurements. The nucleus has to be populated in a way to give states of aligned angular momentum

with a specific orientation in space. This can be done by applying an electric and magnetic field to polarised the nucleus. In a fusion evaporation reaction the angular momentum vector $(l = r \times p)$ is perpendicular to the beam direction [16, 10, 6] as shown in Fig. 3.3. The evaporation of the particles and gamma-rays attenuates the orientation of the nucleus which will provide m-states with $m=0$ corresponding to the reaction plane.

The angular distribution function is [16, 6]

$$W(\theta) = \sum_k A_k P_k(\theta), \tag{3.2}$$

where W(θ) is the gamma-ray intensity measured at angle θ to the beam direction, k is even numbers, $P_k(\theta)$ is the Legendre polynomials and A_k are the angular distribution coefficients.

For a pure dipole $\Delta I = 1$ transition (E1), the angular distribution will be [16, 6]

$$W(\theta) = A_0(1 + A_2 P_2(\cos\theta)), \tag{3.3}$$

where $P_2(\cos\theta){=}\frac{1}{2}(3\cos^2\theta - 1)$.

For a quadrupole $\Delta I = 2$ transition (E2), the angular distribution will be [16, 6]

$$W(\theta) = A_0(1 + A_2 P_2(\cos\theta) + A_4 P_4(\cos\theta)), \tag{3.4}$$

where $P_4(\cos\theta){=}\frac{1}{8}(35\cos^4\theta - 30\ cos^2\theta + 3)$.

The experimental angular distribution can be obtained from the intensities of the gamma-rays as a function of the detectors angles with respect to the beam direction. The value of the A_2 and A_4 coefficients can be found by fitting the angular distribution function applying the equation 3.2. Comparing the experimental and theoretical coefficients leads to the determination of spin and parities.
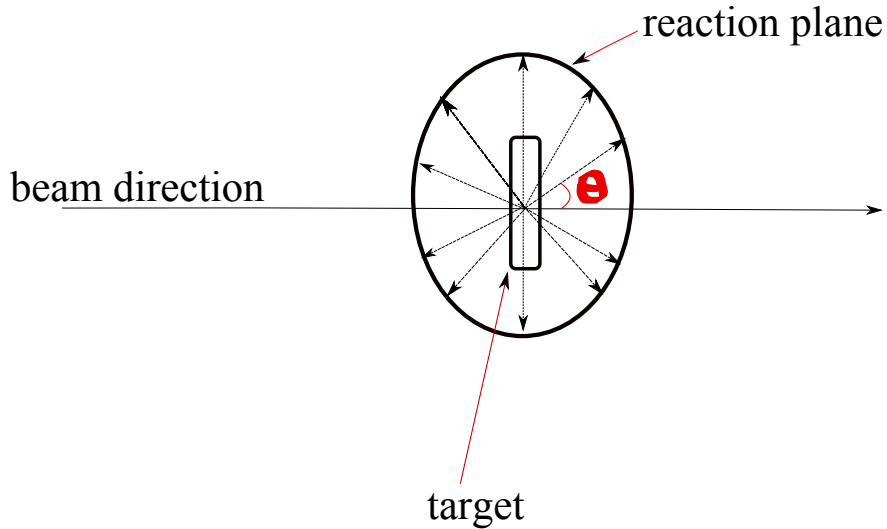
Figure 3.3: Schematic drawing of the angular distribution process. The beam direction is represented by the z axis and θ is the angle between the γ-ray emission and the beam axis [3].

3.2   Recoil Decay Tagging and Recoil Isomer Tagging

In addition to the fusion-evaporation processes there may be strong competition from other reaction processes such as fission. A technique is required to cleanly select the specific reaction channel and to correlate the γ rays to the correct nucleus. Such methodology is *Recoil Decay Tagging* (RDT) which was applied for first time by Simon *et al.* [17] in an experiment in GSI and used by Paul *et al.* [18] with a large

γ-ray spectrometer.

The prompt γ rays, emitted within $10^{-12} - 10^{-9}$ s after the fusion evaporation products were formed, are detected at the target position by HPGe detectors. The fusion products are separated from the unreacted beam in a recoil separator. After separation, fusion events are implanted in double sided Si detectors (DSSD) at the focal plane. The time of flight (TOF) through the separator is typically $\sim 0.5 \ \mu$s. The reaction products pass firstly through the MWPC where energy is deposited and the time recorded. The signal from the MWPC is recorded as the start signal and the DSSD produces the stop signal to generate a TOF - energy loss spectrum that can be used to discriminate recoils from beam particles. The reaction products tend to have higher masses and move more slowly than the beam they deposit more energy in MWPC.

Temporal and spatial correlations between recoil implantations and their decays (usually taken to be $3 \times t_{1/2}$) within the same pixel are used as a selective tag on γ-rays emitted at the target position. However, care should be taken to account for high implantation rates or the long decay half-lives for the channel of interest in order to avoid random correlations. The ^{158}W nucleus studied in this work has ideal decay properties since it decays via emission of an α particle with a distinct energy, short half-life (0.16 ms for 8 $^+$ state) and high branching ratio. Figure. 3.4 shows a schematic representation of the RDT technique.

The *recoil isomer tagging* (RIT) technique works on a similar principle except that γ rays emitted at the target position are correlated with isomer-delayed gamma rays that are detected with the clover or planar detectors at the focal plane.
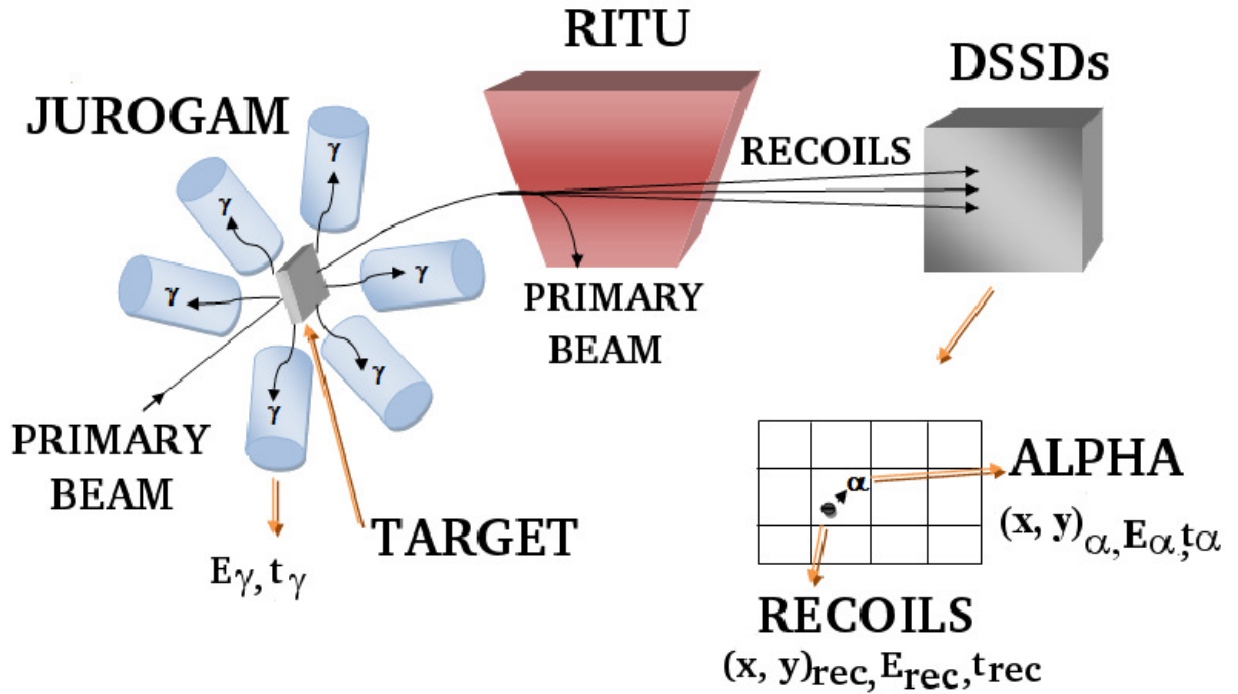
Figure 3.4: The Recoil Decay Tagging technique is illustrated schematically. Identification of the recoil and its subsequent decay can be obtained from the same pixel of a DSSD using temporal and spatial correlations. Delayed coincidences to allow for the flight time of recoils through the separator allow the identification of the γ rays associated with the nucleus of interest.

To obtain information about the nucleus of interest using these techniques, a condition must be set on the α-decay or delayed γ-ray energy that is required. Furthermore, recoils must be discriminated from unreacted/scattered beam using time-of-flight and energy loss measurements between one of more MWPCs or the MWPC and the DSSDs at the focal plane. Figure. 3.5 shows a typical two-dimensional matrix representing the energy loss in the MWPC and the TOF between the MWPC and DSSDs of
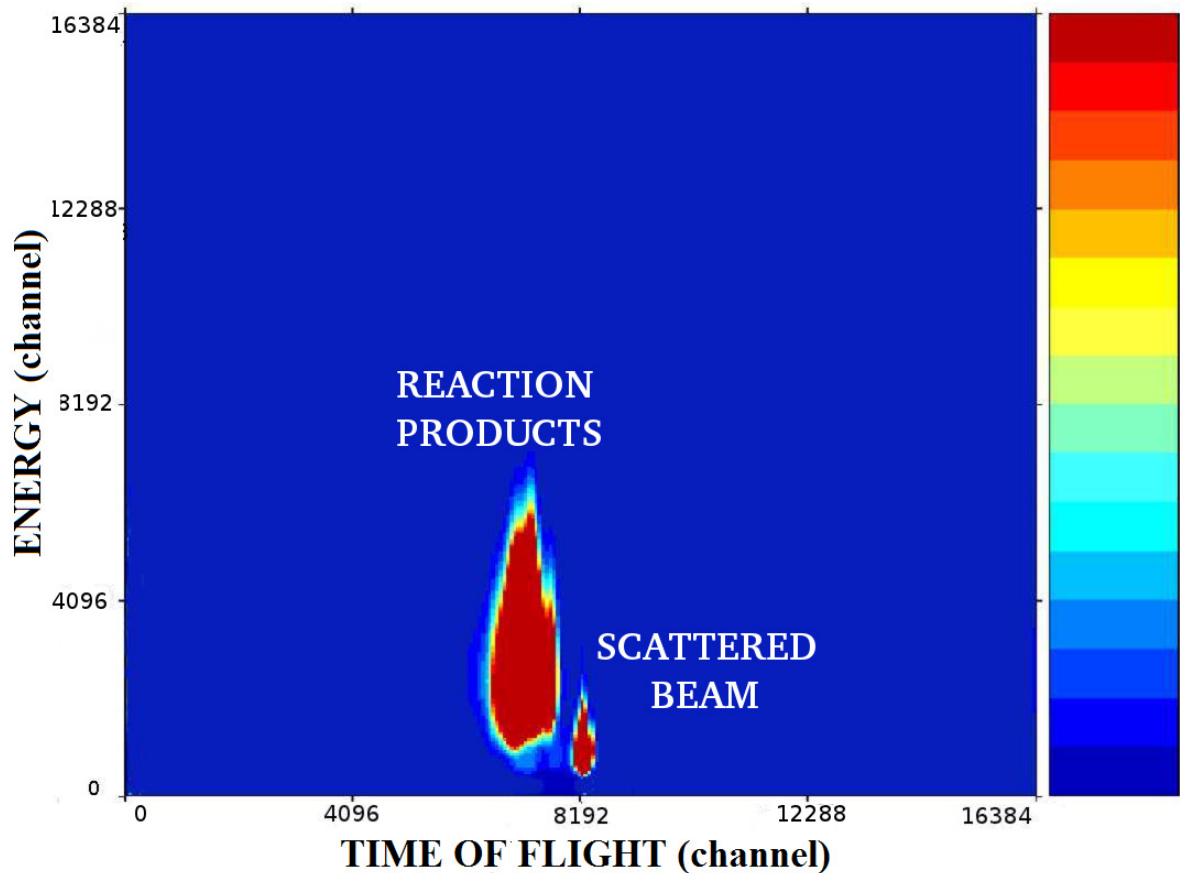
Figure 3.5: Energy loss vs time of flight (TOF). The TOF is determined between MWPC and DSSD.

the GREAT spectrometer. The recoils and unreacted beam are represented by the groupings on the left and right, respectively. A gate is placed around the recoils which is included in the code.

3.3 Gamma-Ray Spectroscopy

In order to detect the γ rays, the photon must first interact with a detection medium. Detectors normally used for detection of γ rays come in two different forms: scintillator and semiconductor. Semiconductor, and in particular HPGe, detectors are normally preferred over the scintillator detectors due to superior energy resolution and their compact size. One disadvantage compared with a scintillator detector is a relatively poor efficiency.

Germanium is a small band gap semiconductor where the electrons are bound to the lattice in a *valence band* and there is a vacant *conduction band* where electrons must be excited to move freely. The energy of the band gap for semiconductors has the value of 0.7 eV while for insulators >5 eV. At the temperature of 0 K, the conduction band is empty and the valence band is full in an intrinsic semiconductor. At high temperature, the electrons from the valence band can obtain enough thermal energy to reach the conduction band leaving holes in a random excitation process. When an electric field is applied the electrons from the conduction band of the neighbour atoms will occupy these holes leaving other holes in valence band in the places from where they left process called *electron − hole pair*. It will be a movement of the electrons in one direction and of the holes in the opposite direction.

Germanium is the most used semiconductor in the construction of nuclear detectors. However, a semiconductor can be donor or acceptor by introducing a pentavalent or trivalent atom. The semiconductor donor is called as n-type whose majority carriers are electrons. The pentavalent atoms with five electrons make electron conduction

with four of the electrons and the fifth becomes free which is conduction electron. The p-type semiconductor called acceptors where the holes are the majority carriers whose impurities are trivalent atoms that have a covalent bond unmet.

The most commonly type of detector used for gamma ray spectroscopy is n-type Ge which is less sensitive to the neutron damage. Fast neutrons are emitted in reactions with projectile above the Coulomb barrier [19]. These neutrons have enough energy to dislocate the Ge atoms from the lattice leading the holes to be trapped in the dislocations. This impairs the charge collection and energy resolution of the detector. The n-type detector has an outer p^+ where the holes are collected. The holes have a shorter collection path in n-type detectors then in p-type where the inner contact is p^+.

In a semiconductor in which a part contains acceptor impurities and the other part contains donor impurities form a junction called $p - n$ junction. A $p - n$ junction is a transition junction where the electrons from part n diffuses in the part p. The electrons occupy the holes in the p part. It is form a flow of electrons which leave the n part to p part where the electrons recombine with the holes forming a low portion of free carriers called depletion zone.

The width of the depletion zone is defined by the following formula [20]

$$d = (\frac{2\epsilon V}{eN})^{1/2},\tag{3.5}$$

where V is the reverse bias voltage, N is the net impurity concentration, ϵ is the dielectric constant, e is the electronic charge. In the depletion zone the charge carriers can be quickly efficiently collected. In semiconductors this zone is typically 2-3 mm.

TRUE COAXIAL

CLOSED-ENDED COAXIAL

CLOSED-ENDED COAXIAL
(BULLETIZED)
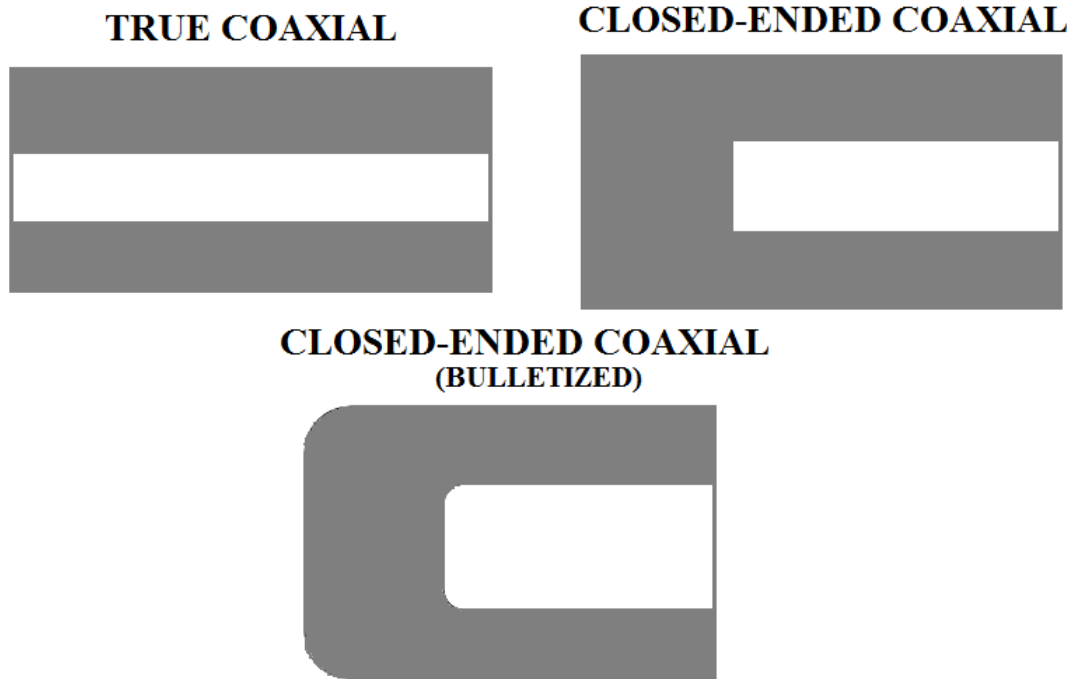
Figure 3.6: A closed ended and a cylindrical geometry of a HPGe detector.

The resistivity of the depletion zone could be increased by applying a reverse bias.

Hyper-Pure Ge (HPGe) detectors are reverse-bias $p-n$ diodes in order to maximise the active depleted region [19]. The HPGe detector with a cylindrical geometry and closed ended configuration is the most commonly used detector in γ-ray spectroscopy. Fig. shows a schematic diagram of a closed ended and a cylindrical geometry of an HPGe detector. This geometry has the advantages that the volume of the detector can be extended and the areas of low electric field which occur at the corners of the closed end can be minimised [20]. The detectors are cooled by LN_2 at temperature of 77 K, but can be stored at room temperature. The cooling is required to reduce the
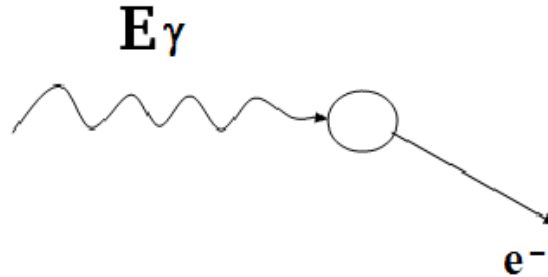
Figure 3.7: The photoelectric interaction of a γ ray with matter.

leakage current.

3.3.1 Gamma-Ray Interactions With Matter

A γ-ray may interact with matter through three primary processes

Photoelectric absorption

Photoelectric absorption (Fig. 3.7) is a process which is important at low energies $(E_\gamma < 500$ keV). A photon is absorbed by a bound electron of the absorber material. The energy of the outgoing electron is given by

$$E_{e^-} = h\nu - E_b, \tag{3.6}$$

where E_b is the binding energy of the photoelectron in its atomic shell and hν is the photon energy. During this process the electron is ejected from the atom leaving
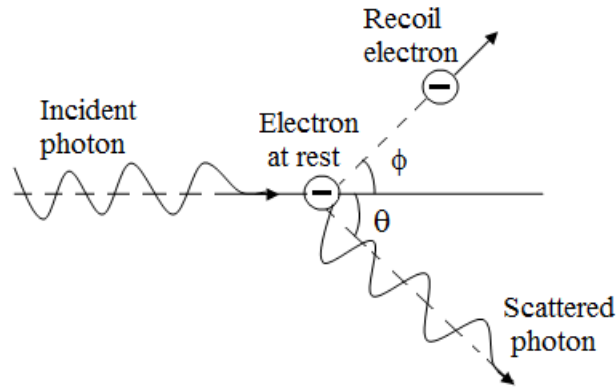
Figure 3.8: Gamma-ray interactions by Compton scattering.

behind a vacancy which will be filled by rearrangements of the other bound electrons. The binding energy is liberated in the form of an X-ray photon or Auger electron. The cross-section for the photoelectric absorption varies with $\sim Z^{4,5}$ [6]. A material with high atomic number is therefore preferred for γ-ray spectroscopy.

Compton scattering

Compton scattering occurs at high energy γ rays in the range 100-1021 keV, see Fig. 3.8. In this process the γ ray is deflected through an angle θ. The energy transferred to the electron depends on the scattering angle. The following equation gives the energy of the scattered γ ray obtained from the conservation of energy and momentum [20]

$$h\nu' = \frac{h\nu}{1 + \frac{h\nu}{m_0 c^2}(1 - \cos\theta)},$$ (3.7)

where the $h\nu$ is the energy of the photon, $m_0 c^2$ is the rest mass energy of the electron

33
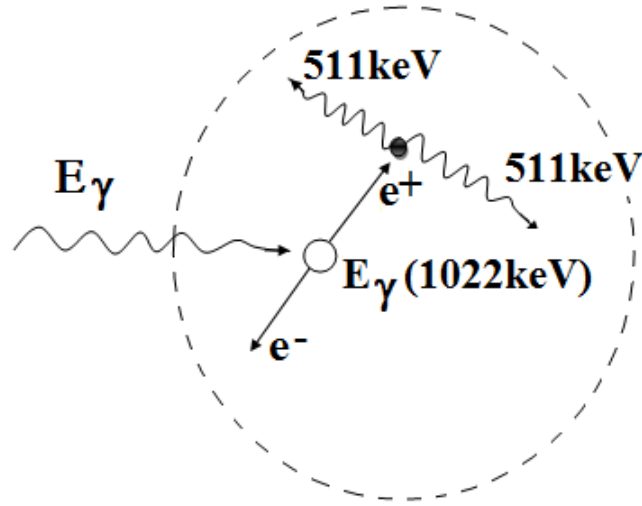
Figure 3.9: The pair production process by which a γ ray may interact with matter.

which has the value of 0.511 MeV.

The cross section of this process varies linearly with the atomic number of the detector material. The angular distribution of the Compton scattering process is given by the Klein-Nishina formula for differential cross section [20]

$$\frac{d\sigma}{d\Omega} = Zr^2 \left(\frac{1}{1 + \alpha(1 - \cos\theta)}\right)^2 \left(\frac{1 + \cos^2\theta}{2}\right)\left(1 + \frac{\alpha^2(1 - \cos\theta)^2}{(1 + \cos^2\theta)[1 + \alpha(1 - \cos\theta)]}\right), \quad (3.8)$$

where $\alpha = h\nu/m_0 c^2$, r is the classical electron radius ($r^2 = 7.94 \times 10^{-26} cm^2$).

Pair production

This phenomenon requires the energy of the incident photon to be twice the rest energy of an electron (1.02 MeV). The photon will interact with the Coulomb field of nuclei in the surrounding medium and spontaneously create an electron-positron pair with a total energy given by the following equation

$$E_{e^-} + E_{e^+} = h\nu - 2m_0c^2. \tag{3.9}$$

The excess energy of the photon above 1.02 MeV is divided between the electron and positron as is shown Fig. 3.9. The positron will subsequently interact with an electron and be annihilated creating two 511 keV photons of which one or both or neither can escape from the medium. If both the photons escape, a double escape peak appears in a γ-ray spectrum. If only one photon escapes while the other is fully absorbed the γ-ray spectrum will display a single-escape peak and if both are absorbed a full energy peak appears. The cross section of the pair-production varies with $\sim Z^2$.

3.3.2   Spectrometer Arrays

In this work the prompt γ rays were detected with the JUROGAM spectrometer array surrounding the target position. The JUROGAM spectrometer consists detectors from EUROGAM Phase I and GASP [19] spectrometer. The crystals of the EUROGAM detector array have a diameter of $\sim$70 mm and length of $\sim$75 mm. The GASP crystals are $\sim$80 mm in length and a diameter of $\sim$72 mm. The Ge detectors are tapered to complete the solid angle in this way the efficiency of the array is improved. The JUROGAM spectrometer operates with 43 coaxial n-type HPGe detectors. The angles of the Ge detectors with respect to the beam direction are presented in Table 3.1. A schematic representation of the angles is drawn in Fig. 3.11.

JUROGAM II represents the next generation spectrometer and consisted of 15 EUROGAM Phase I detectors and 2 rings of 12 fourfold Clover detectors. Table
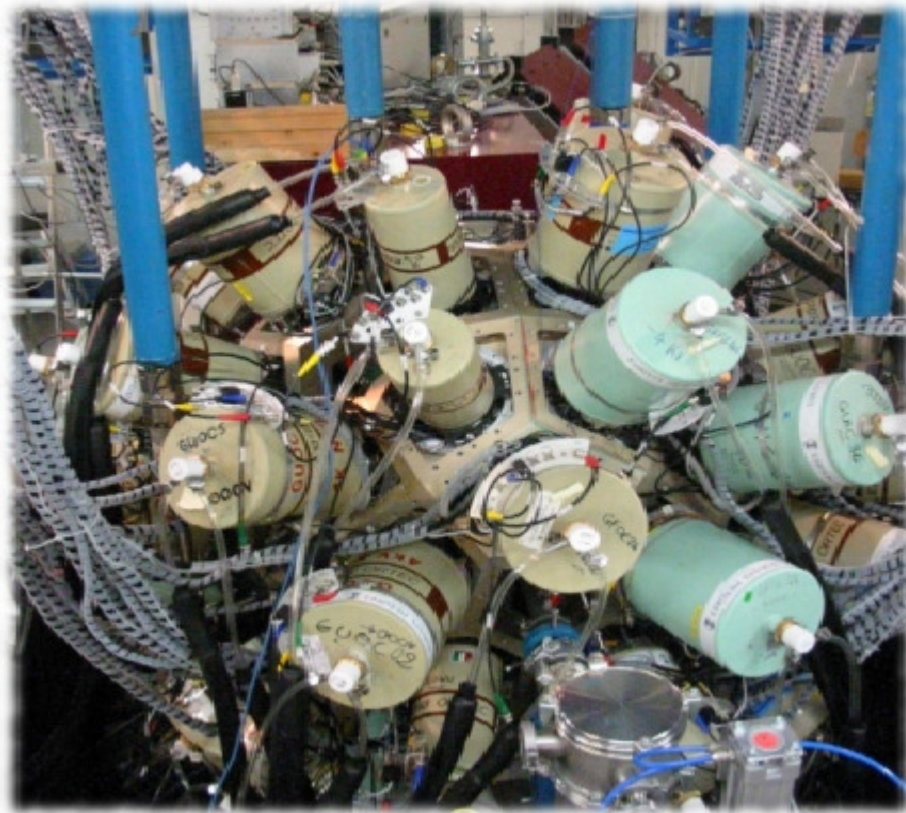
Figure 3.10: The JUROGAM spectrometer array containing 43 n-type HPGe detectors placed in 6 rings surrounding the target [21].

3.2 shows the angles at which are placed the Ge detectors with respect to the beam direction. The dimensions of an n-type Clover are ~ 50 mm in diameter and ~ 70 mm in length. The total photopeak efficiency of the JUROGAM II was boosted from 4.2% to 6% [22].

The Ge detectors are cooled to the temperature of 77 K with liquid nitrogen (LN_2) in order to suppress the thermal excitation of electrons across the band gap. The neutrons from fusion evaporation reactions produce dislocations at temperature ¡
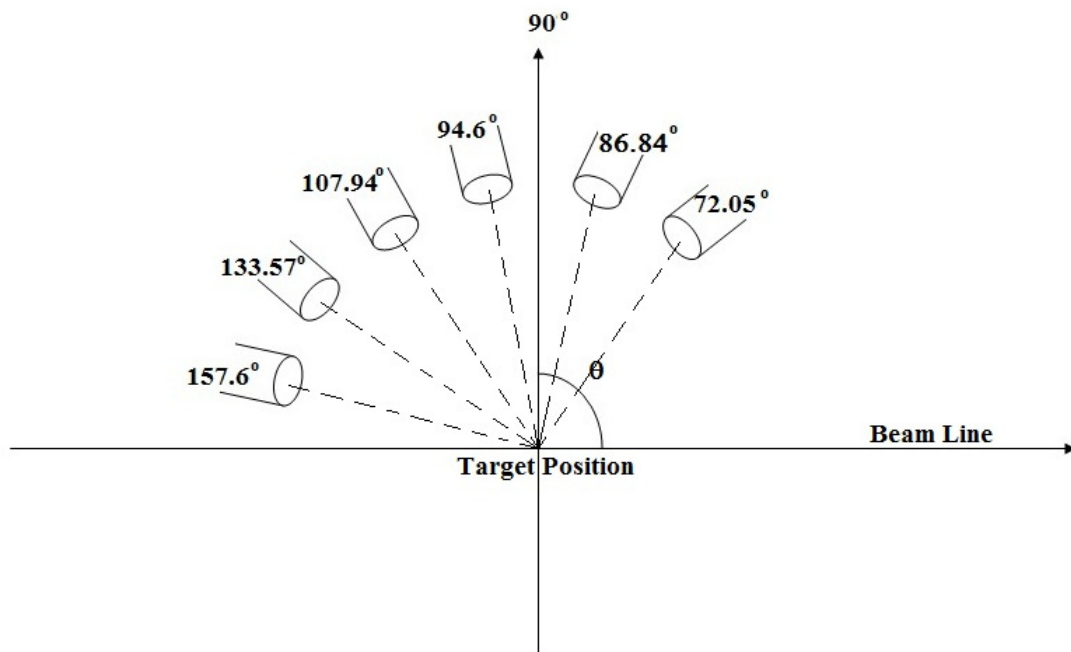
Figure 3.11: The angles of the JUROGAM detectors with respect to the beam line.

130 K by trapping the holes. The hole traps could be remove by annealing the or cooling the detector. The annealing process is done by heating the detector at 105 C for 1–3 hours and keeping the pressure of the cryostat at low pressure ($\sim 10^{-6}$ mbar) [19]. The cooling of detector is through a cold finger in thermal contact with the crystal and a vacuum insulated dewar.

The HPGe crystals are shielded by bismuth germanate-$Bi_4Ge_3O_{12}$-BGO (Fig. 3.12) to reduce the Compton background generated by γ rays scattering out of the detectors. The shields are utilised as a veto by producing an anti-coincidence signal that rejects

Table 3.1: Angular positions and numbers of Ge detectors in the JUROGAM spectrometer. θ is defined with respect to the beam direction.

Ring Number	θ °	Number of detectors
1	157.6	5
2	133.57	10
3	107.94	10
4	94.6	5
5	86.84	5
6	72.05	8

Table 3.2: The JUROGAM II array specifications. θ is defined with respect to the beam direction.

Ring Number	θ °	Number of detectors	Type of the detector
1	157.6	5	Phase I
2	133.57	10	Phase I
3	104.5	12	Clover
4	75.5	12	Clover

the absorbed events. The BGO works in two modes as individual suppression mode when the signal from the Ge detector is suppressed by its own shield and the shared suppression when the signal of a Ge detector is suppressed by its own shield and the
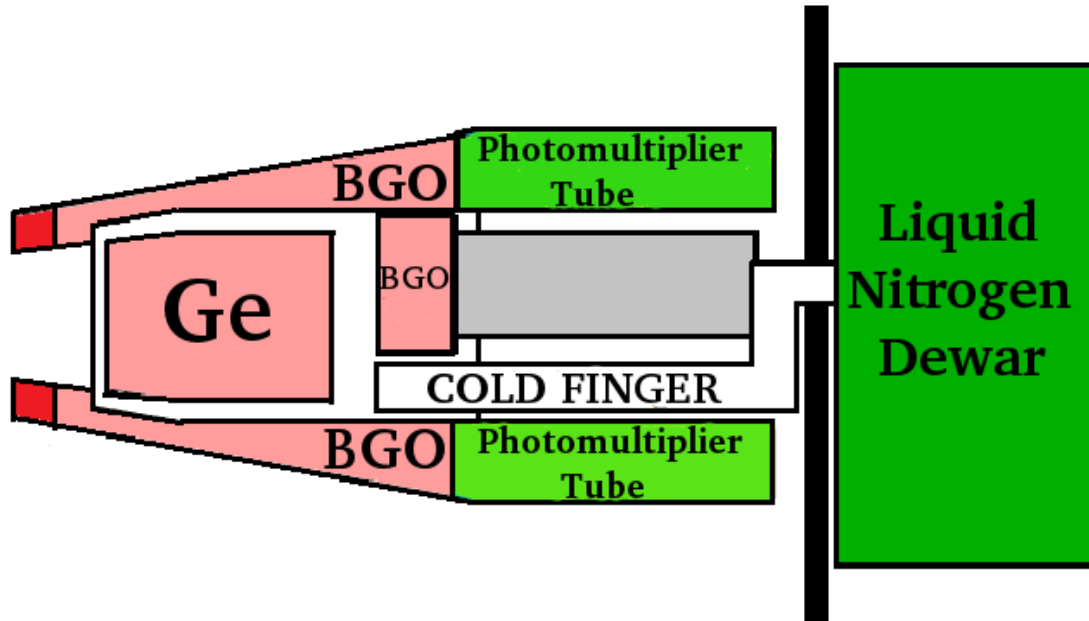
Figure 3.12: A schematic diagram of the BGO shield [23].

BGO of the next ring [24]. The BGO shields are tapered at the front and have a length of 190 mm and a thickness of 18-20 mm [25].

The relative efficiency curve of the JUROGAM (Fig. 3.13) was obtained by placing ^{133}Ba and ^{152}Eu sources inside the target chamber before and after the experiments.

3.4   Recoil Ion Transport Unit separator (RITU)

The Recoil Ion Transport Unit (RITU) is a gas-filled recoil separator used in studies of heavy elements [27]. Its role is to separate the fusion reaction products from other reaction residues and fission. RITU has a QDQQ (Q = quadrupole, D = dipole) magnet configuration as shown in Fig. 3.14, improving the matching of recoils to the
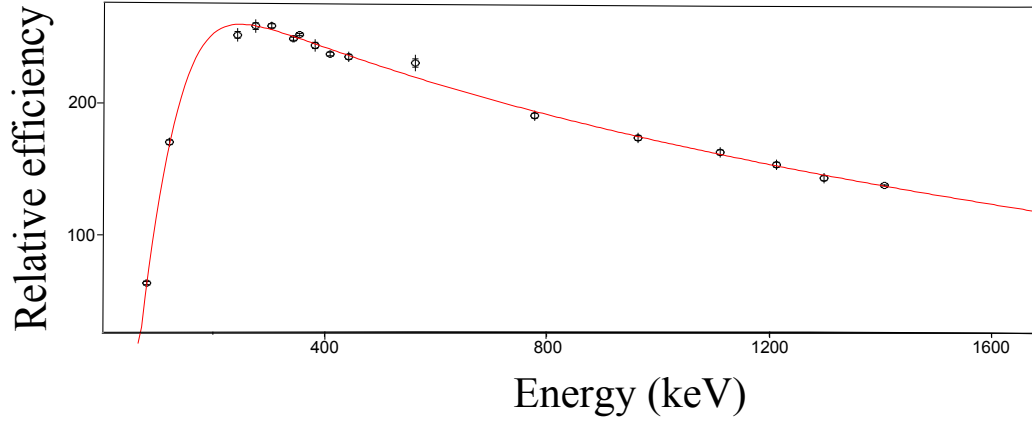
Figure 3.13: The JUROGAM relative efficiency curve as a function of the energy. The efficiency curve was obtained by placing ^{133}Ba and ^{152}Eu sources at the target position.

acceptance of the dipole magnet. The dipole has a deflection angle of 25° and a central radius of curvature of 1.85 m. The unreacted beam is stopped in a tantalum stopper located in the dipole chamber. The separator is filled with helium at pressure up to 0.6 mbar. The angular acceptance of the separator is ±80 mrad vertically and ±30 mrad horizontally. A thin foil of Ni (450 μg/cm^{-2}), C (100 μg/cm^{-2}) or differential pumping system is used to separate the high vacuum of the beam line from the He which fills the region from the target chamber to the focal plane.

3.4.1 Principle of operation

Recoil ions will slow down and undergo atomic collisions when they pass through the RITU separator. As result of collisions, the electrons can be captured or lost,
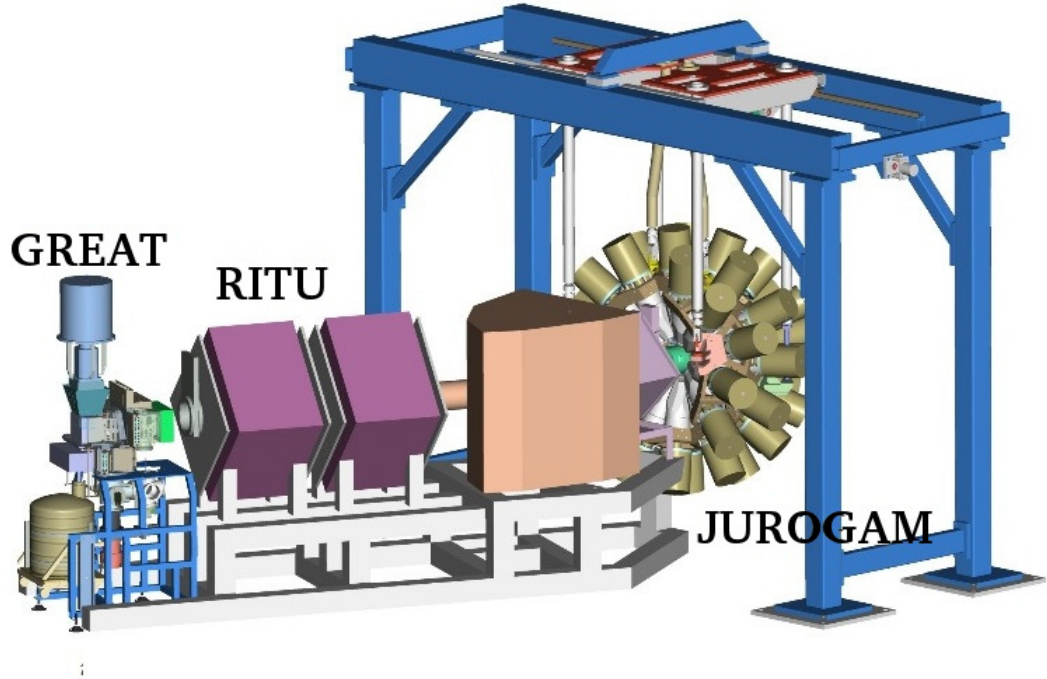
Figure 3.14: The JUROGAM-RITU-GREAT apparatus. The target is surrounded by the JUROGAM HPGe spectrometer array followed by the RITU separator and the GREAT detector at the focal plane. The configuration of the RITU separator is one quadrupole magnet followed by a dipole magnet and two focussing quadrupole magnets [26].

which results in an average charge state. They will follow a trajectory given by the average charge state as shown in Fig. 3.15. Consider an ion with mass m moving with a velocity v in a magnetic field with the direction perpendicular to the field of flux B it will follow a circular path of radius ρ.

The magnetic force, being perpendicular to the velocity, provides the centripetal force which has the following equation
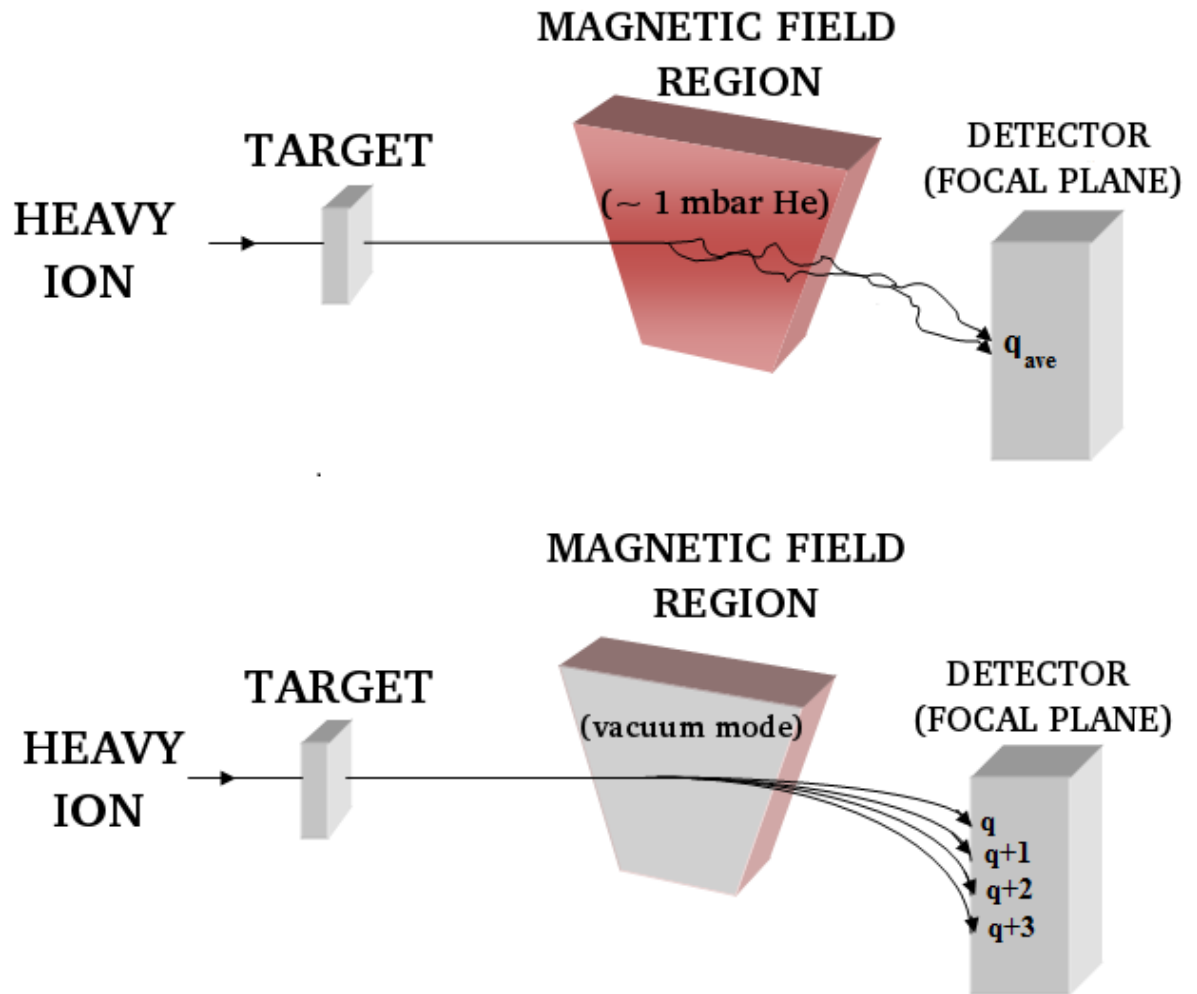
Figure 3.15: A gas separator separates the fusion evaporation reactions from the beam and fission products. The recoiling nuclei follow an average path due to charge exchange collisions with the gas.

$$F = ma = \frac{mv^2}{\rho} = qvB \Rightarrow B\rho = \frac{mv}{eq}. \tag{3.10}$$
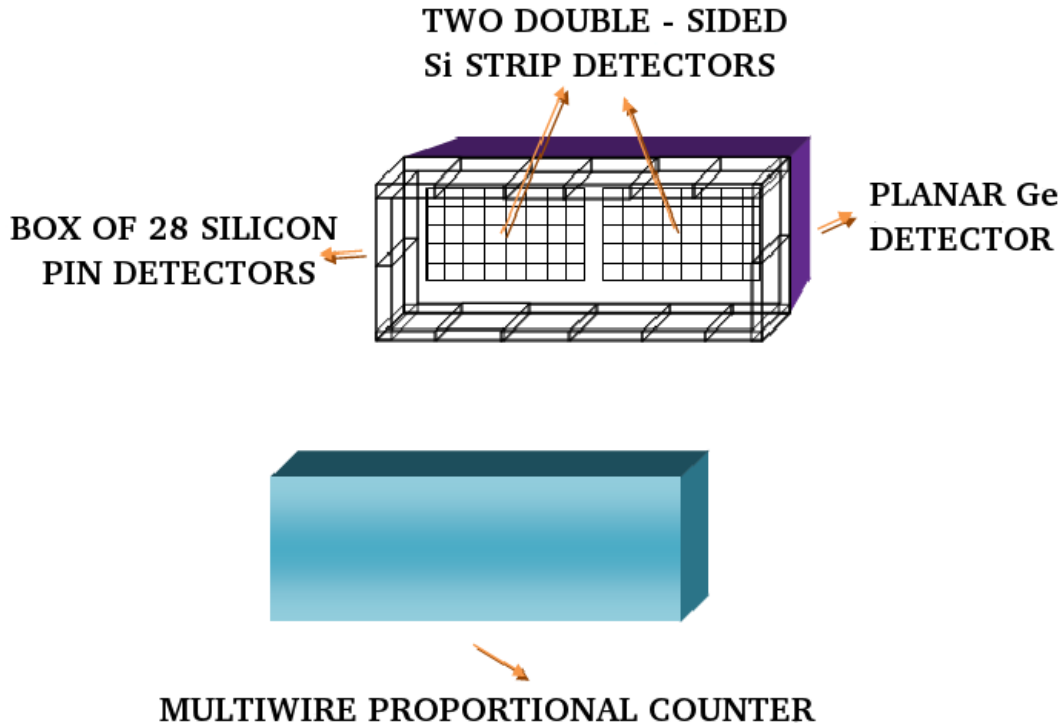
Figure 3.16: The MWPC which is the first detector of the GREAT spectrometer with the purpose to distinguish between the recoils and their decay. This detector gives information about energy loss, timing and position of the recoils.

The Thomas - Fermi model of atom [28] approximates the average charge as

$$q = \frac{v}{v_0} Z^{1/3}. \tag{3.11}$$

The new equation for the magnetic rigidity it will be [29]

$$B\rho = \frac{mv_0}{eZ^{1/3}} = \frac{Auv_0}{eZ^{1/3}} = 0.0227 \frac{A}{Z^{1/3}}. \tag{3.12}$$

where m can be written as Au, u is the atomic mass, A mass number, e is the elementary charge and $v_0 = \frac{h}{2\pi mr}$ is the Bohr velocity, which has the value of 2.19×10^6

43

m/s. RITU is a mass separator with a maximum magnetic rigidity of 2.2 Tm.

3.5 GREAT

The Gamma Recoil Electron Alpha Tagging (GREAT) [30] spectrometer is located at
the focal plane of the RITU separator. The following subsections discuss the properties
of the GREAT spectrometer components.

3.5.1 MultiWire Proportional Counter (MWPC)

The MWPC (Fig. 3.16) has dimensions of 131 mm horizontally and 50 mm vertically
being the first detector of the GREAT spectrometer. An isobutane volume is separated
from the helium gas of RITU and the vacuum at which other detectors of GREAT
work by Mylar windows. The purpose of the MWPC is to distinguish between the
recoils and their subsequent decays. Also, this detector measures energy loss, timing
and position signals of the implanted recoils. A low level of scattered beam reaches
the focal plane and they can be confused with the evaporation residues so a time of
flight between the DSSDs and MWPC is required to suppress scattered beam [30].

3.5.2 Double Sided Silicon Strip detectors (DSSDs)

The principal detector of the GREAT spectrometer is the Double Sided Silicon Strip
Detectors (DSSDs). The function of the DSSDs is to measure the energy of the recoils
and properties of their decays (α, fission, β and protons). The GREAT spectrometer
is provided with two side-by-side silicon strip detectors as shown in Fig. 3.16. Each

DSSD has the dimensions of 60 mm x 40 mm with a thickness of 300 μm [30]. The strip pitch of 1 mm in both directions gives a total of 4800 pixels for both silicon detectors. The distance between the GREAT DSSDs is 4 mm thus maximising the geometric efficiency of the detector in order to collect $\sim$85 % of the reaction products. The DSSDs are cooled by circulating alcohol at -20°C to to ensure an optimum energy resolution is achieved.

3.5.3 PIN detector

The PIN (Fig. 3.16) diode detectors can be used to detect the conversion electrons or escaping α particles from the DSSDs. In total there are 28 silicon PIN diodes surrounding the DSSDs. The PINs are cooled by the same refrigeration system as the DSSDs. Each of the PIN diodes has an area of 28 mm $\times$ 28 mm and a thickness of 500 μm.

3.5.4 Planar germanium strip detector

The planar detector of the GREAT spectrometer is used for the detection of low-energy γ rays ($\sim$ 10 keV to 600 keV), high energy β particles and X-rays. It is mounted behind the DSSDs and has an active area of 120 mm $\times$ 60 mm and a thickness of 15 mm. The planar Ge strip detector has 12 horizontal and 24 vertical strips with a strip pitch of 5 mm on both sides. The detector has a beryllium entrance window and it is mounted inside a vacuum chamber to minimise the attenuation of low-energy photons.
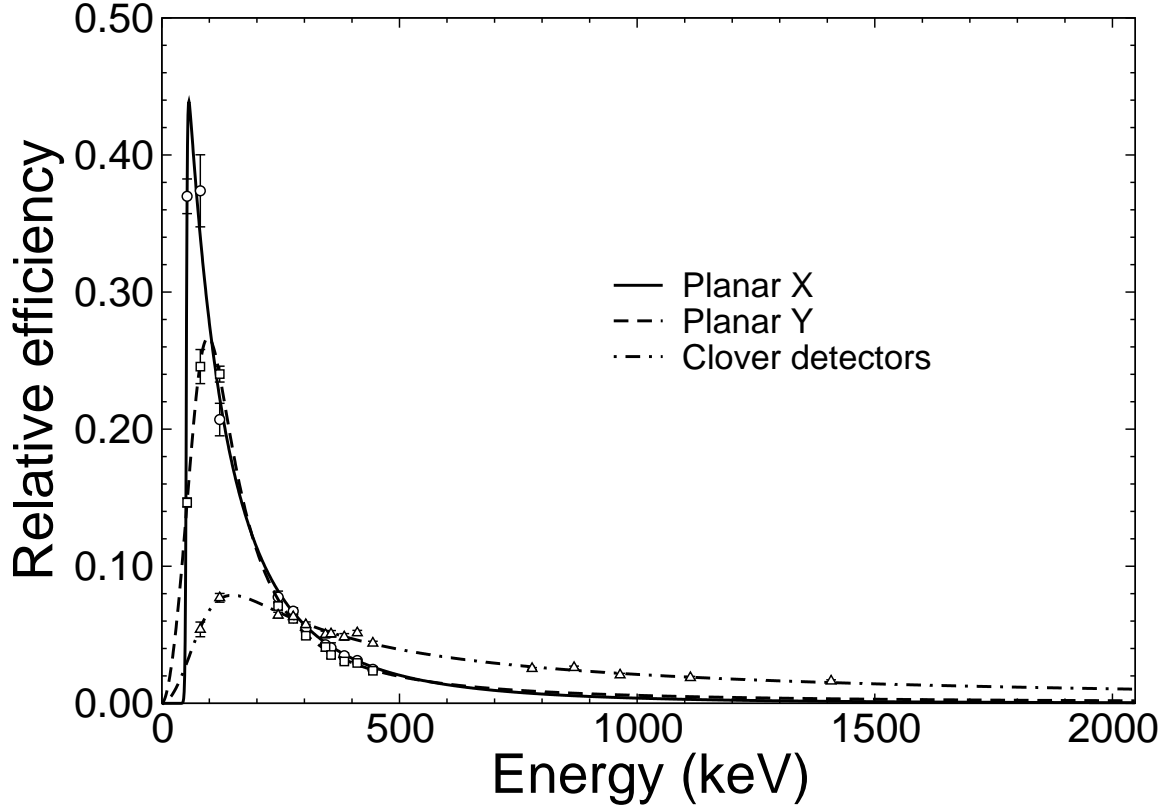
Figure 3.17: The efficiency curve for the HPGe detectors placed at the focal plane.

3.5.5 Clover Germanium Detector

The clover detector(s) is(are) mounted outside the vacuum chamber and are designed to detect high-energy photons from ~ 100 keV to 5 MeV. The detectors contain four n-type Ge crystals enclosed in a common cryostat. A crystal has a diameter of 70 mm before shaping and is 105 mm long. The crystal is narrowed towards one end at an angle of 30°. The close distance between the Ge crystals (~ 0.2 mm) improves the

add-back factor in which γ rays Compton scattered between the four detectors are added into the full-energy peak. Each Ge crystal is divided in another four segments to improve the granularity of the detector. Figure 3.17 represents the efficiency curve as a function of energy of the various focal plane detectors. It is observed that the planar detector is more efficient for energies up to 300 keV. Planar X and Planar Y, although they share the same piece of Germanium, are different strips located on a different part of the detector and so there are differences that affect their efficiency. In particular, the X strips are on the front (RITU and DSSD facing) and the Y strips are on the back. This has a very noticeable effect when looking at X rays as they do not penetrate very far into the Germanium. Because they deposit energy closer to the X strips, the charge collection of the X strips is more efficient than for the Y strips (Imagine electrons having to drift across only a short distance, as opposed to a longer distance). This is not so noticeable at higher energies, where the relative energy efficiencies are similar for X and Y strips. It is probably also the case that the amount of Germanium covered by the X strips differs to the Y strips, which again will have an effect on the efficiency.

3.6   Total Data Readout

The Total Data Readout (TDR) [31] is a trigger-less data acquisition system that reads all the detector channels independently. The system reduces the common dead time. All data collected is time stamped with a precision of 10 ns by a 100 MHz clock. A schematic of the GREAT TDR and data acquisition system is presented

in Fig. 3.18. In TDR the data is filtered against unwanted data, consists of vetoed and piled up signals, through analogue – to – digital – converters (ADC) [15]. The software developed to analyse the raw data is GRAIN [15] which is based on JAVA programming language. The data is composed of two types of events: recoils and decays.The recoils are detected n DSSDs detectors. The decays of the recoils are detected in the same pixel of the DSSDs and correlated with the prompt γ-rays from the target plane. The correlation is obtained with application of time and energy conditions.

TARGET POSITION
Ge array

MWPC PIN   Si Strips   Ge Strips   Segmented large
Ge

NIM + CAMAC + shape amps + CFDs

6 TACs | 364 energy | 370 gates | 32 bits

METRONOME → VXI time stamping ADCs   Hit patern

SHARC Links

DATA BUFFERING

Gigabit Ethernet

EVENT BUILDER

Data to
tape
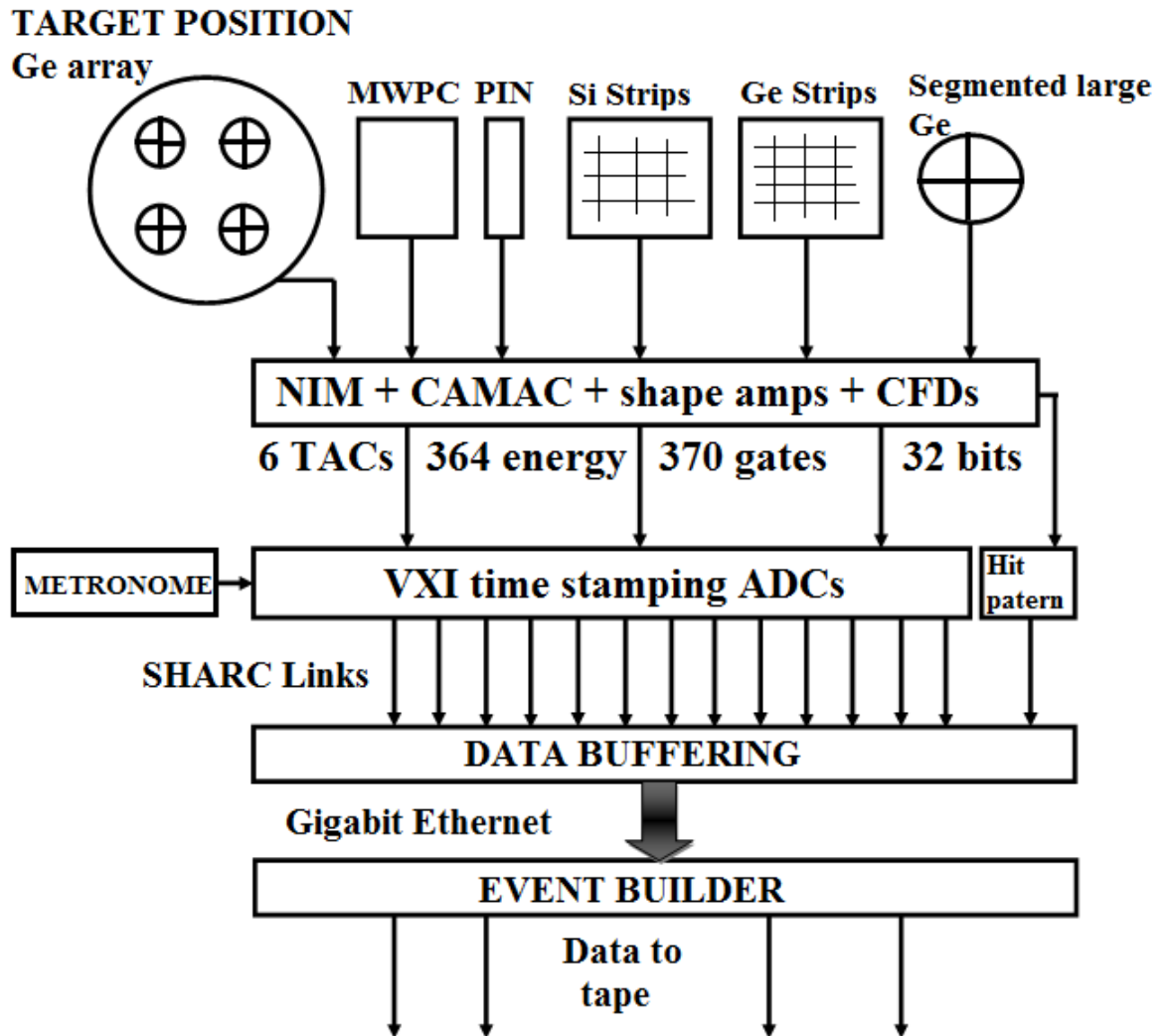
Figure 3.18: A schematic diagram of the GREAT TDR system's electronics and data acquisition.

Chapter 4

First observation of excited states in ^{158}W

Excited states in the neutron-deficient nuclide ^{158}W were investigated using the ^{102}Pd(^{58}Ni,2n) reaction ($E_{beam} = 280$ MeV) in an experiment performed at the University of Jyväskylä Accelerator Laboratory. The level scheme for ^{158}W has been established for the first time using γ-ray coincidences correlated with the characteristic α decays from the ground state and isomeric 8^+ state of ^{158}W. The ground state band has the form of a shell model multiplet and is established to a tentative (6^+) state. Several γ-ray transitions have been built upon the isomeric 8^+ state. Configurations for the new structures are discussed in terms of excited neutron $f_{7/2}$ and $h_{9/2}$ configurations and in the context of shell model calculations.

4.1　Motivation

Understanding how the structure of heavy nuclei evolves towards shell closures is a long standing goal of nuclear physics. Systematic investigations of energy level schemes across the isotope chains reveals the evolution from collective structures near the neutron midshell towards single-particle multiplets near the closed shells. The measurement of excited states in heavy neutron-deficient nuclei near the N=82 closed shell and the proton drip line is challenging from a γ-ray spectroscopy perspective. The production cross sections of nuclei with around 20 fewer neutrons than the lightest stable isotope are very low (μb level or lower). Also the large γ-ray backgrounds originating from other reactions channels obscure the weaker signals from the most neutron-deficient reaction channels. The background can be suppressed by using highly selective experimental methods such as the recoil-decay tagging technique. This technique has allowed the excited states to be discovered in many of the neutron-deficient W-Os-Pt nuclei below the Z=82 shell gap [32, 33, 34, 35, 36, 37, 38].

Figure 4.1 shows the ratio of the 4^+ and 2^+ states in the even-even neutron-deficient Hf, W and Os isotopes. The $E(4^+)/E(2^+)$ ratio reveals the change in collective behaviour from deformed rotational nuclei at the mid-shell ($N = 104$), through γ-soft shapes towards vibrational excitations. The ratio of the 4^+ and 2^+ for the ^{158}W calculated in the present work is 1.84 and represented in the figure 4.1. The ratio of the two energies is dropping as neutron closed shell is approach. This is evidenced in the ^{158}W nucleus which has two neutrons far from the closed neutron shell $N = 82$.
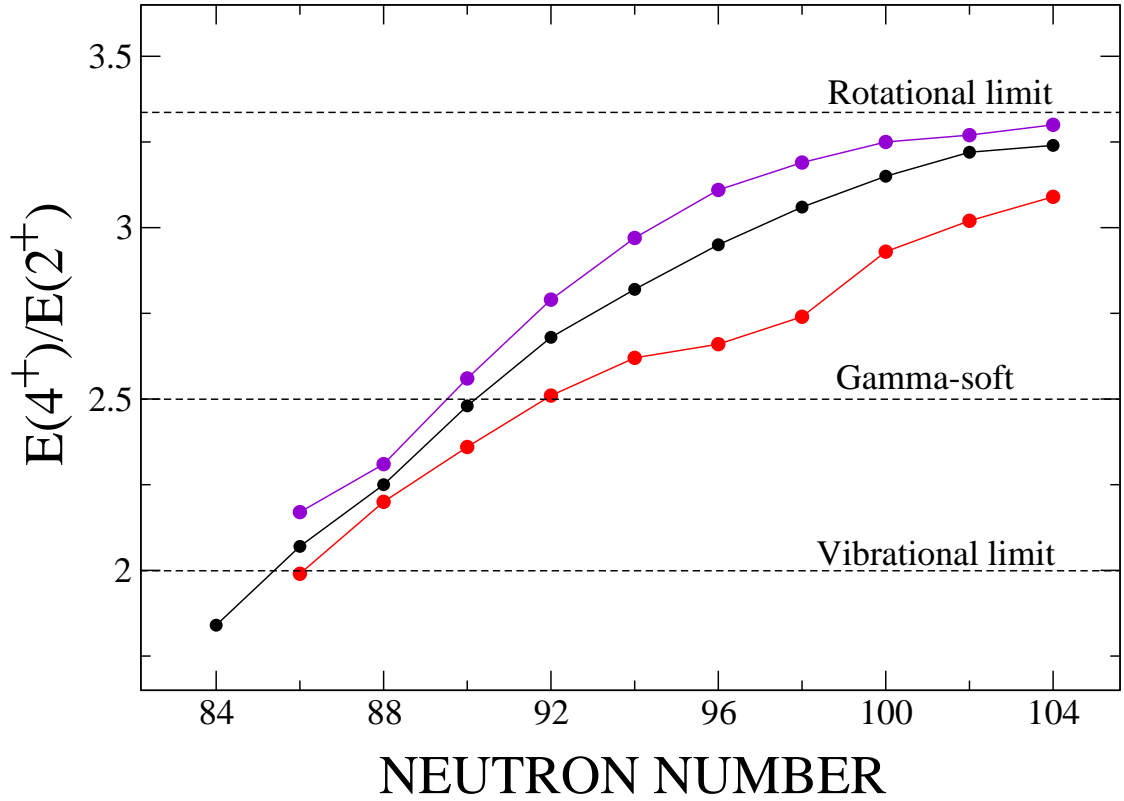
Figure 4.1: The E(4$^+$)/E(2$^+$) ratio in function of the neutron number for the Os (red circle), W (black circle) and Hf (purple circle) nuclei [32, 39, 40, 41, 42, 43, 44, 45, 35, 33, 46, 47, 48, 49, 50, 51, 52, 53, 54, 55, 56, 57].

Nearer to the closed neutron shell at $N = 82$, the angular momentum of excited states is expected to be generated by aligning the spins of a small number of valence nucleons, which should be reflected in the level schemes.

It has been established that the structure of the light W isotopes is sensitive to the occupation of specific core-polarising orbitals near the Fermi surface [58]. Figure 4.2

shows representative proton and neutron Nilsson diagrams for the W isotopes. The proton Fermi surface lies in a region of low level density near the high-Ω $h_{11/2}$ states. The neutron Fermi surface lies above the $N = 82$ shell gap close to the high-j, lowest-Ω $i_{13/2}$ orbital and negative-parity orbitals originating from both the $f_{7/2}$ and $h_{9/2}$ subshells. The yrast structures in the even-N W isotopes with neutron numbers greater than ^{164}W are mostly built on configurations involving the $i_{13/2}$ neutron orbital [40, 41, 58, 42]. Figure 4.2 shows that as the average deformation decreases towards the closed $N = 82$ shell, the negative-parity $f_{7/2}$ and $h_{9/2}$ states are more likely to form the yrast configurations. This was observed in the ground-state band of ^{162}W, where Dracoulis et $al.$ [59] noted that the first rotational alignment was at a lower frequency than observed in the heavier even-N isotopes and concluded that the $h_{9/2}$ neutron orbitals are responsible for the alignment.

Investigations of near spherical nuclei near closed shells can provide constraints on the relative positions of the single-particle orbitals near the Fermi surface. This chapter aims to elucidate the structure of the highly neutron-deficient nuclide ^{158}W, which has two neutrons outside the $N = 82$ closed shell and likely to be based on excitations of the negative-parity neutron states.

4.2 Previous work

The exotic nucleus ^{158}W was first discovered by Hofmann et $al.$ [60] in radioactive decay spectroscopy measurements performed using the SHIP velocity filter at GSI. Hofmann observed two α-decays in correlated decay chains corresponding to ^{158}W.
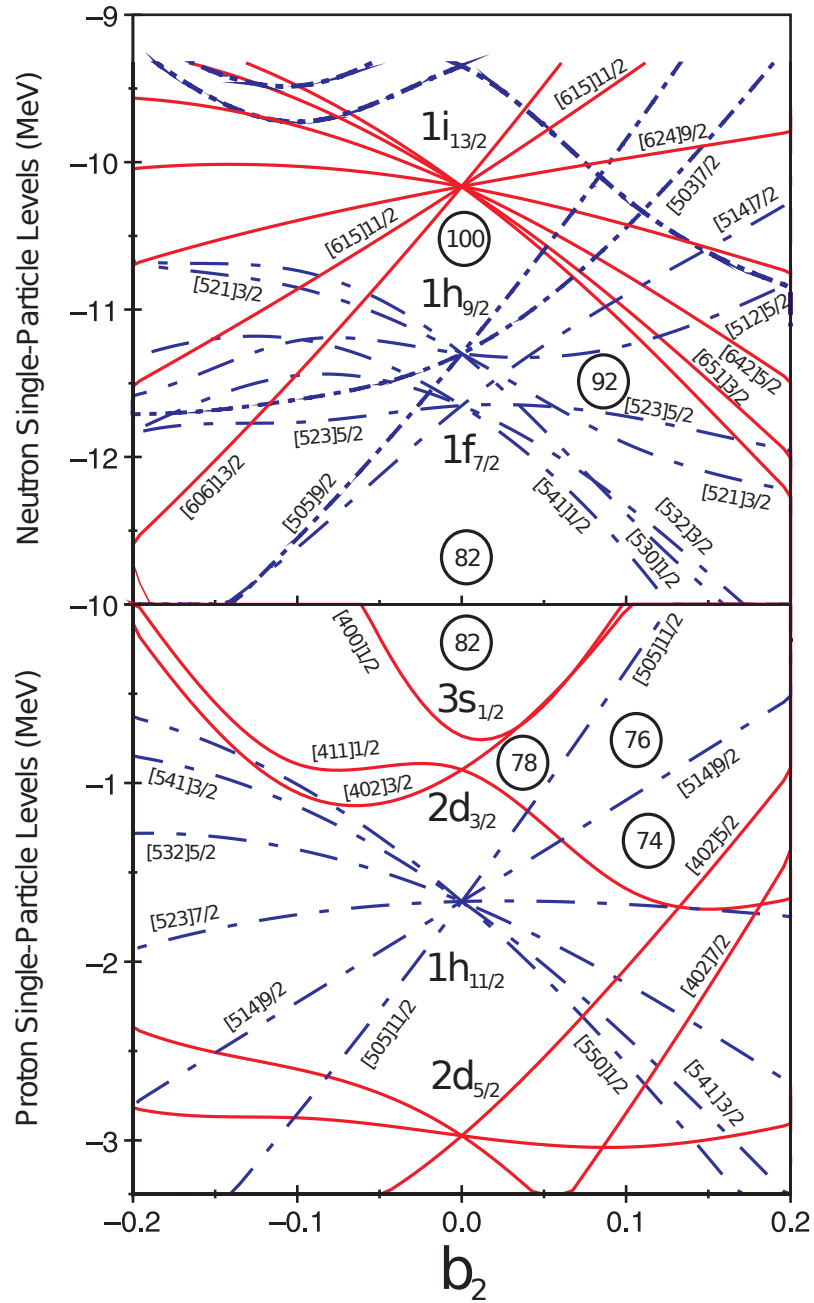
Figure 4.2: The Nilsson diagram for protons and neutrons as a function of deformation parameter β_2. The positive-parity levels are marked by a solid red line and the negative-parity levels are represented by dashed blue lines.

The α decay from the ground state was identified with an energy E_α =6442±21 keV and half-life $t_{1/2} = 0.9$±0.3 ms. The α decay from the isomeric state was observed at an energy E_α =8280±30 keV and half-life limited to the range $t_{1/2}$ =(0.01-1) ms. Page *et al.* [61] confirmed the α decays in an experiment at the recoil separator at Daresbury and provided a firm measurement of the half-life of α-decay from the isomeric state at $t_{1/2} = 0.16$±0.05 ms [61]. The isomeric state was fixed at an excitation energy of 1849 keV.

Seweryniak *et al.* [37] performed an experiment to investigate excited states in the $N = 84$ isotones ^{156}Hf, ^{157}Ta and ^{158}W using the ^{102}Pd(^{58}Ni,xp2n) reaction. The prompt γ rays were detected with the Gammasphere array of Compton suppressed HPGe detectors. The recoils were separated from the beam with the Argonne fragment mass analyzer and implanted in a DSSD where their subsequent radioactive decays were identified. A singles γ-ray spectrum correlated with the characteristic α decay from the 8^+ isomeric state led to the observation of three low intensity γ rays at 204 keV, 478 keV and 1074 keV. A level scheme could not be constructed since there were insufficient statistics to allow a γ-ray coincidence analysis. No γ-ray transitions based on the ground state were observed in this experiment.

This chapter reports the results of an experiment aiming to investigate the $N = 84$ isotones at the University of Jyväskylä Accelerator Laboratory. The experiment has sufficient statistics to permit the first observation of the excited-state multiplet based on the ground state and the construction of a level scheme above the isomeric 8^+ state through a γ-ray coincidence analysis.

4.3 Experimental Details

Excited states in ^{158}W isotones were populated using the ^{102}Pd(^{58}Ni,xp2n) reaction at a beam energy of 280 MeV. The target was a 500 μg/cm^2 thick, self-supporting ^{102}Pd foil. An average beam current of 6 pnA. Gamma rays were detected at the target position by the JUROGAM γ-ray spectrometer [62] consisting of 43 EUROGAM-type escape-suppressed germanium spectrometers [62]. Recoiling fusion-evaporation residues were separated from the unreacted beam and fission fragments by the RITU gas-filled recoil separator [27] and deposited into the double-sided silicon strip detectors of the GREAT spectrometer [30] at the focal plane. Recoiling nuclei were distinguished from the residual scattered beam and radioactive decays by energy loss and (in conjunction with the DSSDs) time of flight methods using the GREAT multiwire proportional counter.

All detector signals were passed to the total data readout (TDR) acquisition system [31] where they were time stamped with a precision of 10 ns to allow accurate timing correlations between γ rays detected at the target position, recoil implants at the focal plane and their subsequent radioactive decays. These trigger-less data were sorted into γ-ray spectra and γ-γ matrices using GRAIN [15] and analysed with the RADWARE software packages [63].

4.4 Results

The recoil-decay tagging technique provides high-confidence correlations between γ rays and subsequent radioactive decays provided that the implantation rate is low in

comparison to the half-life of the correlating decay. Usually the implantation rate should be no greater than one implantation every 3-5 half-lives. The nucleus ^{158}W has ideal decay properties for this method since both decays have relatively short half-lives, high α-decay branching ratios and, in the case of the 8^+ decay, a distinctive decay energy. The half-lives of the α decays in ^{158}W are short in comparison to the average recoil rate 2 kHz.

Figure 4.3 shows the particle decay spectrum obtained from the DSSD. The fusion evaporation reaction produces many open exit channels. This spectrum highlights the challenge in identifying γ-ray transitions in ^{158}W due to the low production cross section of the $2n$ exit channel. The characteristic α decays of ^{158}W are not obvious from the main spectrum. The inset shows an expanded region of the same spectrum indicating the presence of the ^{158}W-α decays.

4.4.1 Excited states built on the ground state

It may been seen from Fig. 4.3 that the ground-state α decay lies on the large background originating from the tail of the α decay from the 25^- isomer in ^{155}Lu. This presents challenges for the identification of excited states built upon the ground state. However, it has been possible to identify γ-ray transitions feeding the ground state using the recoil-decay tagging technique. Figure 4.4(a) shows γ rays correlated with a recoil implanted in the GREAT spectrometer followed by the characteristic α decays of ^{158}W within the same pixel. The search time for correlations was limited to 2.7 ms ($\sim 3 \times t_{1/2}$). It is apparent that this spectrum is heavily contaminated by γ-ray transitions from ^{155}Lu, which are present due to the correlations with the background
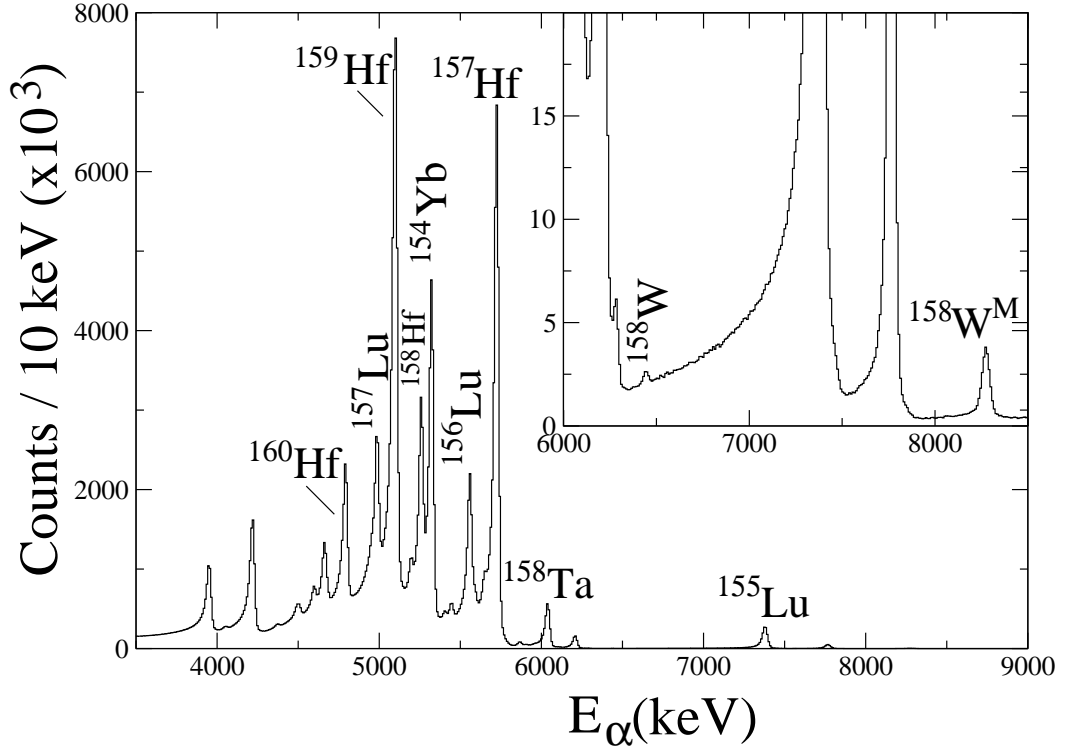
Figure 4.3: Particle decay energy spectrum of all decays.

tail. There are also several γ-ray peaks that are not assigned to the level scheme of ^{155}Lu.In order to assess the nature of the ^{155}Lu background the same methodology was applied by tagging on the ^{155}Lu tail at the high-energy side relative to the ^{158}W ground-state α-decay. Fig. 4.4(b) shows γ-ray transitions correlated with the background (centred on $E_\alpha = 7390\pm5$ keV) with recoil-decay correlations limited to 2.7 ms. The γ-ray transitions in ^{155}Lu are clearly identified in this correlation however, the new γ-rays observed in the ^{158}W gate are not present suggesting that these transitions belong to ^{158}W. Fig. 4.4(c) shows the background subtracted spectrum generated by subtracting a normalised spectrum Fig. 4.4(b) from 4.4(a). The normalisation was
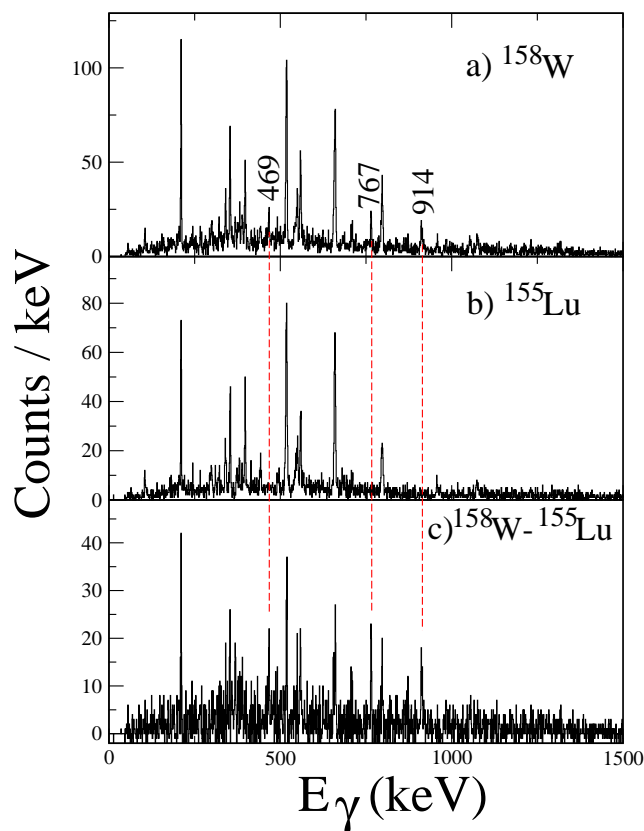
Figure 4.4: (a) Gamma rays correlated with recoil implantations followed by the characteristic ground-state α decay within the same DSSD pixel of the GREAT spectrometer. The correlation time was limited to 2.7 ms. (b) Gamma rays correlated with recoil implantations followed by the α decays in the low-energy tail of the ^{155m}Lu α decay within the same DSSD pixel of the GREAT spectrometer. The correlation time was limited again to 2.7 ms. (c) Gamma-ray spectrum correlated with the ground state α decay of ^{158}W as in part (a) with the background generated by the correlations in part (b) subtracted.

Table 4.1: Relative intensities of γ rays assigned to feed the ground state in ^{158}W. Intensities were obtained from a tagged singles γ-ray spectrum. The γ-ray intensities are normalised to the 914 keV transition.

Eγ (keV)	Iγ (%)
469	67± 13
767	85±14
914	100±18

performed with respect to the highest peak in the background spectrum 518 keV. Figure 4.4(c) allows the identification of three new γ rays at 469 keV, 767 keV and 914 keV. These γ-ray transitions are assigned to feed the ground state of ^{158}W. It was not possible to perform a γ γ-coincidence analysis due to the low statistics. The γ rays are assumed to form a cascade and are ordered on the basis of the relative intensities of the γ-ray transitions, see Table 4.1.

4.4.2 Excited states built on the isomeric 8^+ state

The α-decaying isomeric state in ^{158}W has been interpreted as an 8^+ state based on the $(h_{9/2})^2$ or $(f_{7/2} \otimes h_{9/2})$ neutron configuration [61]. The $E_\alpha = 8280$ keV decay line corresponds to the decay from this 8^+ isomer and is clearly seen in the inset of Figure 4.3. The decay is not obscured by decay peaks originating from other reaction channels and has ideal decay properties ($t_{1/2}$=0.16±0.05 ms, $b_\alpha \sim 100\%$) for recoil decay tagging. Figure. 4.5 shows γ rays correlated with a recoil implanted in the

Figure 4.5: Gamma rays correlated with recoil implantations followed by the α decay from the 8^+ isomeric state within the same DSSD pixel of the GREAT spectrometer. The correlation time was limited to 480 μs. Not all the γ rays could be placed in the level scheme due to the low counts.

GREAT spectrometer followed by the characteristic α decay of the 8^+ isomer in ^{158}W within the same pixel. The search time for correlations was limited to 480 μs,which corresponds to $\sim 3 \times t_{1/2}$.Four intense γ-ray transitions are apparent in the spectrum at 204 keV, 476 keV, 843 keV and 960 keV, which have been observed for the first time. There were sufficient statistics to allow a $\gamma\gamma$-coincidence analysis to be performed. Figure 4.6 shows γ rays in coincidence with the 204 keV, 476 keV, 843 keV transitions

Table 4.2: Relative intensities of γ rays assigned to feed the 8^+ isomeric state in ^{158}W. The relative intensities have been measured from a tagged singles γ ray spectrum and have been normalised with respect to the intensity of the 843 keV transition.

Eγ (keV)	Iγ (%)
204	40$\pm$ 4
476	78$\pm$ 7
843	100$\pm$ 10
960	63$\pm$ 7

and 960 keV, respectively.

There is evidence that all the γ rays listed above are in mutual coincidence. The absence of the 960 keV transition in the spectrum in coincidence with the 204 keV transition is likely to be due to the low efficiency for detecting high-energy γ rays over 900 keV. Figure 4.7 shows the deduced level scheme for ^{158}W; the transitions are ordered according to their relative intensities listed in Table 4.2. It is interesting to note that the 204 keV and 476 keV transitions were also observed in the earlier Gammasphere experiment by Sewerynia*et al.* [37]. The tentative γ-ray transition at ∼1074 keV transition that was reported by Seweryniak is also confirmed in this work although it could not be placed in the level scheme.The intensity of the γ rays feeding the 8^+ isomeric state is presented in the Table 4.2. The deduced level scheme for ^{158}W is shown in Fig. 4.7.

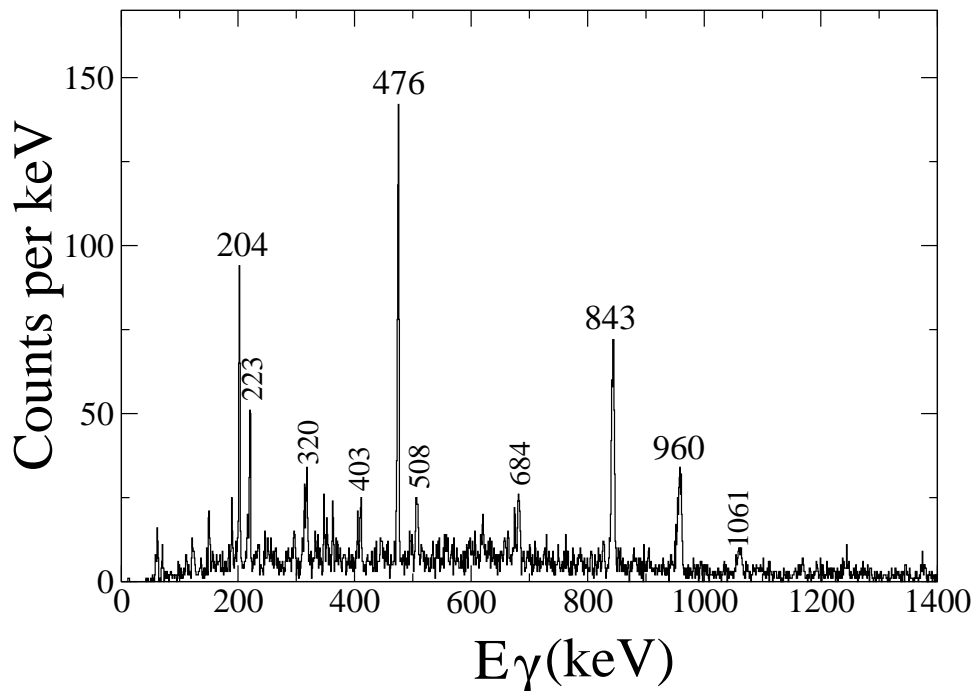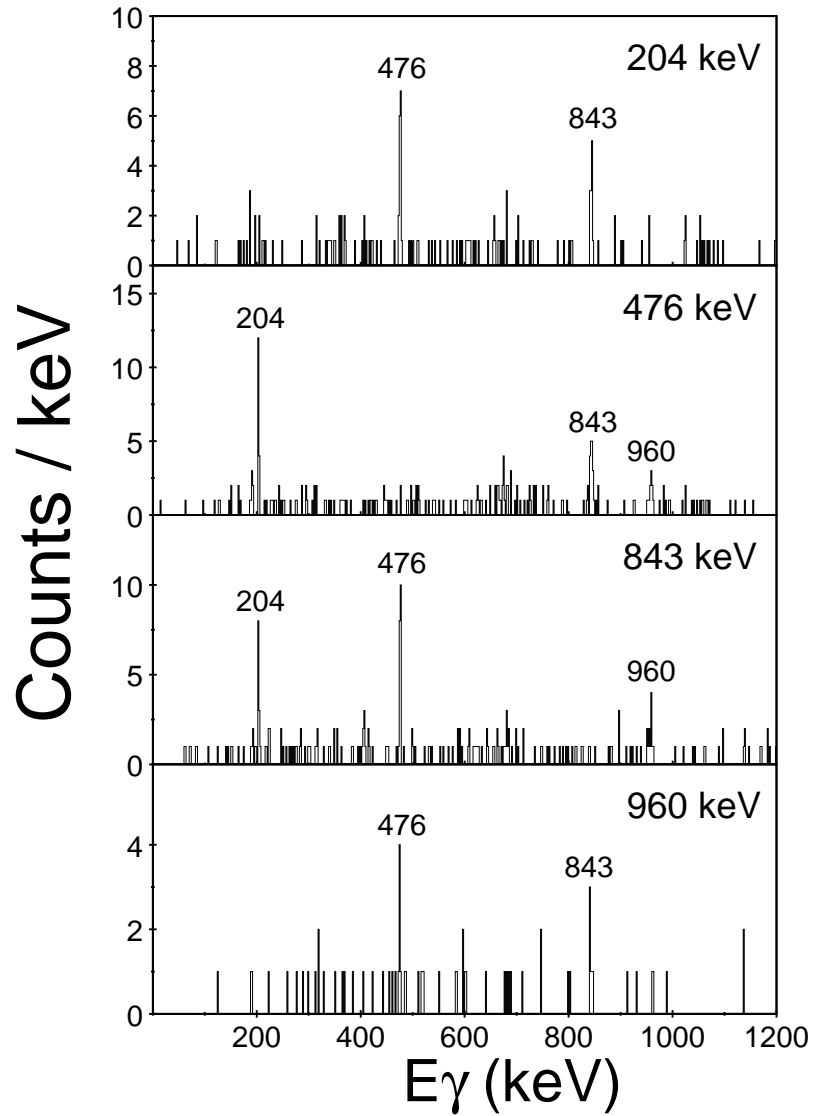Figure 4.6: Typical γ-ray coincidence spectra correlated with recoil implantations followed by the α decay from the 8^+ isomeric state within the same DSSD pixel of the GREAT spectrometer. The correlation time was limited to 480 μs. Gamma rays in coincidence with: (a) the 204 keV γ ray. (b) the 476 keV γ ray. (c) the 843 keV γ ray. (d) the 960 keV γ ray.
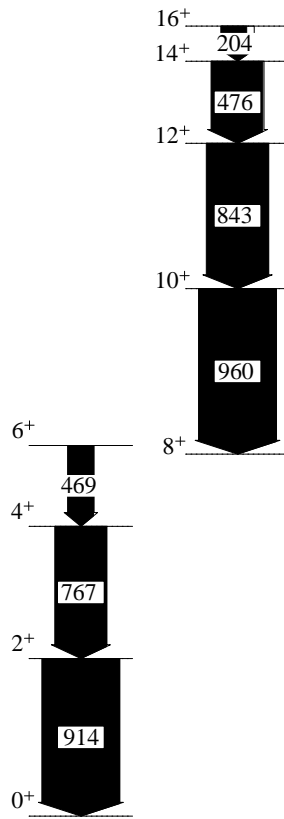
Figure 4.7: The level scheme deduced for ^{158}W. The transition energies are given in keV and their relative intensities are proportional to the widths of the arrows. The excitation energy of the 8^+ state relative to the ground state is deduced from α decay measurements.

4.5 Discussion

The level structure of ^{158}W indicates that the angular momentum of the excited states is likely to be generated by aligning the spins of the valence particles.
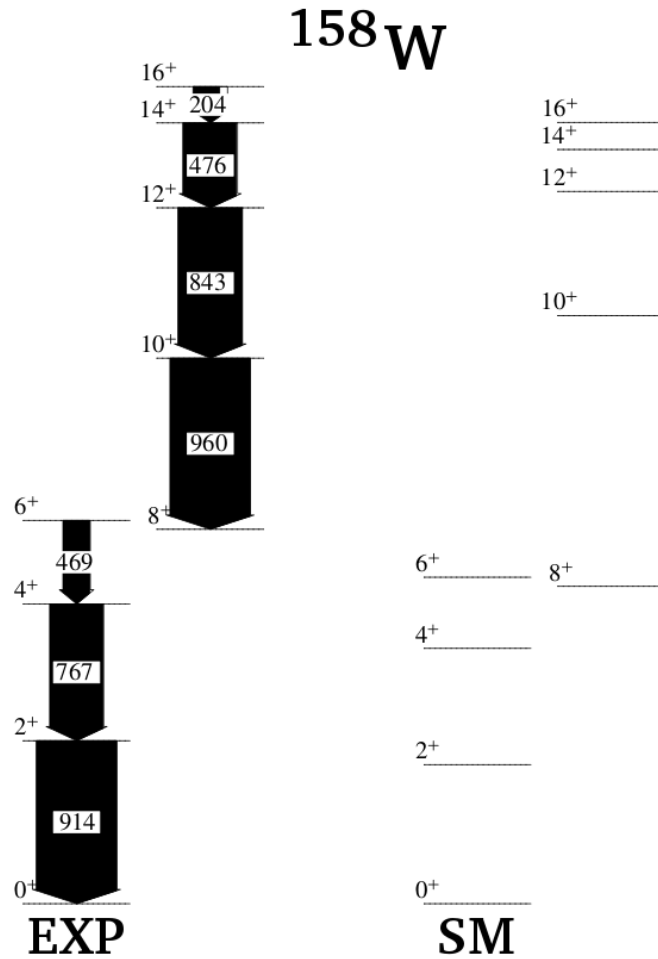
Figure 4.8: The experimental level scheme (on the left) deduced for the ground state and isomeric 8^+ state of ^{158}W. The transition energies are given in keV and are compared with the level scheme produced with the OXBASH code (on the right). The level scheme includes the relative intensities which are proportional to the widths of the arrows.

Due to the close proximity of this nucleus to the closed neutron shell at $N = 82$ it is probable that the negative-parity neutron orbitals will figure prominently in the

excited state configurations. To aid configuration assignments shell model calculations have been performed using the OXBASH code [64]. The shell model calculations assume a ^{146}Gd ($Z = 64$, $N = 82$) core and use single-particle energies and two-body matrix elements taken from Ref. [65]. Calculations were performed for $(f_{7/2})^2$ and $(f_{7/2}, h_{9/2})$ neutron configurations for comparison with the structures based on the ground and isomeric states, respectively. The experimental level scheme obtained for ^{158}W is compared with the predictions of the spherical shell model in Fig. 4.8. There is good agreement between the experimental data and the OXBASH calculations. The calculations were performed with 10 protons in $h_{11/2}$ and 2 neutrons in $f_{7/2}$. The levels selected to be put in the experimental level scheme are the levels with the lowest of a given spin. The shell model calculations for the $(f_{7/2})^2$ configuration reproduces the approximate spacing of the excited states into a multiplet based on the ground state. The cascade feeding the ground state is observed to a tentative 6^+ state at an excitation energy of $E_x = 2150$ keV, which is the maximum permitted angular momentum for an aligned neutron pair in the $f_{7/2}$ orbital. On the basis of these calculations the ground-state cascade is assigned an $(f_{7/2})^2$ configuration. The calculations for $(f_{7/2}, h_{9/2})$ neutron configurations reproduce the relative positions of the 8^+ isomeric state to the fully aligned 6^+ $(f_{7/2})^2$ configuration. The ordering of states in ^{158}W in the level schemes reflects the emergence of specific nucleon excitations. The inversion of the 6^+ and 8^+ states originates from an attractive spin-orbit interaction between the $h_{11/2}$ protons and $h_{9/2}$ neutrons, which increases as the number of protons in the $h_{11/2}$ subshell increases [65]. This interaction is responsible for the decrease in the excitation energies of the $h_{9/2}$ orbitals (and configurations involving the $h_{9/2}$) with respect to

the low-lying $f_{7/2}$ excitations. This has been observed experimentally in the level schemes of the even-Z $N = 84$ isotone ^{156}Hf and the even-Z $N = 86$ isotones such as ^{160}W [32] and ^{162}Os [35]. The lowering of the $h_{9/2}$ orbital is also observed in the inversion of the $25/2^-$ and $27/2^-$ states in the even-Z $N = 83$ isotones from ^{147}Gd to ^{153}Yb [66] and odd-Z $N = 84$ isotones [65, 67, 68]. While the calculations are based on $(f_{7/2}, h_{9/2})$ neutron couplings, the fully aligned $(h_{9/2})^2$ configuration is also a possible candidate for the structure of the 8^+ state. The states above the isomeric 8^+ state are produced by breaking a proton pair from the $h_{11/2}$ subshell and coupling with the $(f_{7/2})^2$ neutron orbitals giving a maximum angular momentum up to 16^+.

The excited states identified in ^{158}W fit in with the smooth variation of the systematics of low-lying excited states as a function of neutron number in the even-mass tungsten isotopes shown in Fig. 4.9. The energy levels show a fairly regular spacing of all levels at and above $N = 98$. The energies of the 2^+, 4^+, and 6^+ states show a gradual increase in excitation, below $N = 96$ reflecting the lower average deformation with increasing proximity to the $N = 82$ closed shell. The lowering of the 8^+ state excitation energy is a well established trend in the heavy $N = 84$ isotones and is clearly observed in the the W isotopes below $N = 88$. A similar although less pronounced trend is seen for the 10^+ states suggesting that the $h_{9/2}$ neutron orbital is also involved in the configuration. There is an increase in the excitation energy of the 14^+ state assuming that the 476 keV and 204 keV are indeed stretched quadrupole transitions and represent the $14^+ \rightarrow 12^+$ and $16^+ \rightarrow 14^+$, respectively. This increase reflects the energy cost in aligning successive pairs of high-j orbitals.
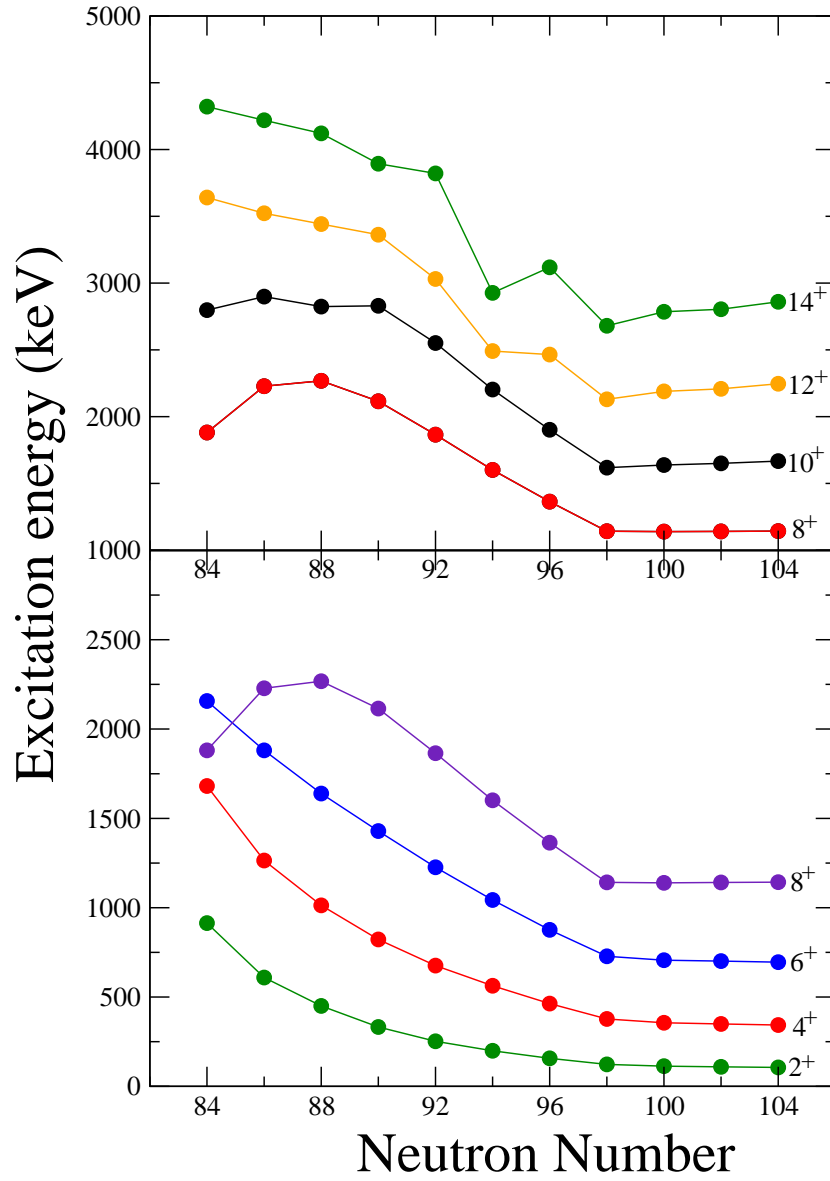
Figure 4.9: The excitation energy as a function of the neutron number in the even-mass tungsten isotopes. The data was taken from Ref.[69],[37],[70] and the present work.

4.6 Summary

Gamma rays emitted from excited states in the neutron-deficient nucleus ^{158}W have been identified using the recoil decay tagging technique. A level scheme has been established for the first time including γ-ray cascades based on the ground and isomeric 8^+ states. The configurations have been interpreted in terms of the OXBASH shell model calculations.

Chapter 5

High-spin states above the 10^+ isomer in ^{152}Yb

Excited states in the neutron-deficient nuclide ^{152}Yb were investigated using the ^{92}Mo(^{64}Zn,$2p2n$) reaction (E_{beam} = 280 MeV) in an experiment performed at the University of Jyväskylä Accelerator Laboratory. New excited states were established above the 10^+ microsecond isomer for the first time using γ-ray coincidences correlated with the isomer-delayed 1531 keV $2^+ \rightarrow 0^+$ γ-ray transition in the ground-state band. Configurations for the new structures are discussed in terms of excited $h_{11/2}$ proton configurations coupled to $s_{1/2}$ and $d_{3/2}$ proton configurations and octupole phonons. The results are discussed in the framework of OXBASH shell model calculations.

5.1 Motivation

Tests of shell model predictions in heavy nuclei were advanced by the discovery that ^{146}Gd exhibits properties that resemble those of doubly magic ^{208}Pb. The similarities were made apparent by the discovery of a low-lying 3^- state [71] in the excitation spectra with a strong $\pi h_{11/2}d_{5/2}^{-1}$ character. The magicity of ^{146}Gd was confirmed by the observation of the 2^+ state, which at 1.97 MeV was approximately 300 keV higher than the other $N = 82$ isotones [72]. These important works provide evidence for a pronounced shell close at $Z = 64$ between the $2d_{5/2}$ and $1h_{11/2}$ proton orbitals. Since these discoveries there has been considerable experimental and theoretical interest in the structure of the N=82 isotones led to detailed experimental studies of neighbouring nuclides in order to characterise (multi)-quasiproton configurations and constrain the shell model.

Considerable progress has been made in understanding the structure of the low-spin states in the heavy $N = 82$ isotones via γ-ray spectroscopy. While the first excited states in ^{146}Gd are based on the $h_{11/2}d_{5/2}^{-1}$ and $h_{11/2}g_{7/2}^{-1}$ proton-hole excitations, above the $Z = 82$ shell gap excitations involving the partially filled $h_{11/2}$ proton sub-shell become important. The even-spin positive-parity states are generated by the alignments of $h_{11/2}$ protons ($\pi h_{11/2}^n$) where n is the number of protons in the $h_{11/2}$ subshell. This configuration can generate a maximum spin up $I^\pi = 10^+$, which forms a seniority $\nu = 2$ microsecond isomer for all the heavy even-even $N = 82$ isotones.

However the yrast configurations in ^{148}Dy ($Z = 66$) and ^{150}Er ($Z = 68$) are dominated by negative-parity states both above and below the 10^+ isomer [71].

Figure 5.1 shows the low-spin states in the heaviest known even-even $N = 82$ isotones from ^{148}Dy to ^{154}Hf and highlights that the yrast intensity flows from the 10^+ isomer through the odd-spin negative-parity states. The lowest odd-spin negative-parity state is the 3^- state, which is formed by coupling the ground state configuration to an octupole phonon arising from the interaction between the $h_{11/2}$ and $d_{5/2}$ ($\Delta l = 3$) proton orbitals. The 5^- and 7^- states are based on the $\pi(h_{11/2})^{n-1}s_{1/2}$ and $\pi(h_{11/2})^{n-1}d_{3/2}$ configurations, respectively. Figure 5.1 suggests that there is a gradual rise in excitation energy of the negative parity states relative to the 2^+ state with increasing proton number.

In contrast to the $\nu = 2$ seniority configurations below the 10^+ isomer very little is known about the higher spin $\nu \geq 4$ excited states in the heavy $N = 82$ isotones. This is partly due to the typical problems of low production cross sections and large γ-ray backgrounds arising for other intense reaction channels including fission. The nucleus ^{150}Er ($Z = 68$) has the most comprehensive level scheme of the heavier $N = 82$ isotones and extends to high spin and an excitation energy of 9509 keV [73]. However, even for this nucleus it was not possible to determine the spins and parities of excited states and level assignments up to 16^+ were made on the basis of comparisons with shell model calculations. It is clear from the work on ^{150}Er by Chung *et al.* [73] that the couplings of $h_{11/2}$ protons figure prominently in the structure of excited states above the 10^+ isomer. This chapter aims to identify the high-spin states in the proton-rich $N = 82$ isotone ^{152}Yb ($Z = 70$) and determine the effect of filling the $h_{11/2}$ subshell on the relative positions of high-spin states along the yrast line.

5.2 Previous work

The first identification of excited states below the 10^+ isomer in ^{152}Yb was made by Nolte *et al.* [74] in beta decay measurements. A major obstacle to understanding the structure of the $N = 82$ isotones via γ-ray spectroscopy is that it is difficult to assign multipolarities of γ-ray transitions that depopulate the microsecond isomer. This problem has been mitigated by later measurements by Nisius *et al* [75] who determined the total internal conversion coefficients and used intensity balance arguments for three of the six transitions in the isomer decay path, see Fig. 5.1. Nisius *et al.* [75] also reported a weak 1889 keV $3^- \rightarrow 0^+$ gamma-ray in parallel with the 359 and 1531 keV transitions. No excited states were established above the 10^+ isomer prior to this work.

5.3 Experimental Details

Excited states in ^{152}Yb were populated using the ^{92}Mo(^{64}Zn,2p2n) reactions at a beam energy of 280 MeV. The target was a 1 mg/cm^2 thick, self-supporting ^{92}Mo foil. An average beam current of 4 pnA was used to bombard the target. Gamma rays were detected at the target position by the JUROGAM II γ-ray spectrometer [62] consisting of 2 rings of 12 CLOVER and 15 EUROGAM-Phase I detectors. Recoiling fusion-evaporation residues were separated from the unreacted beam and fission fragments by the RITU gas-filled recoil separator [27] and transported via a double multiwire proportional counter to a passive stopper at the focal plane. Recoiling nuclei were distinguished from the residual scattered beam and radioactive decays by energy loss and time of

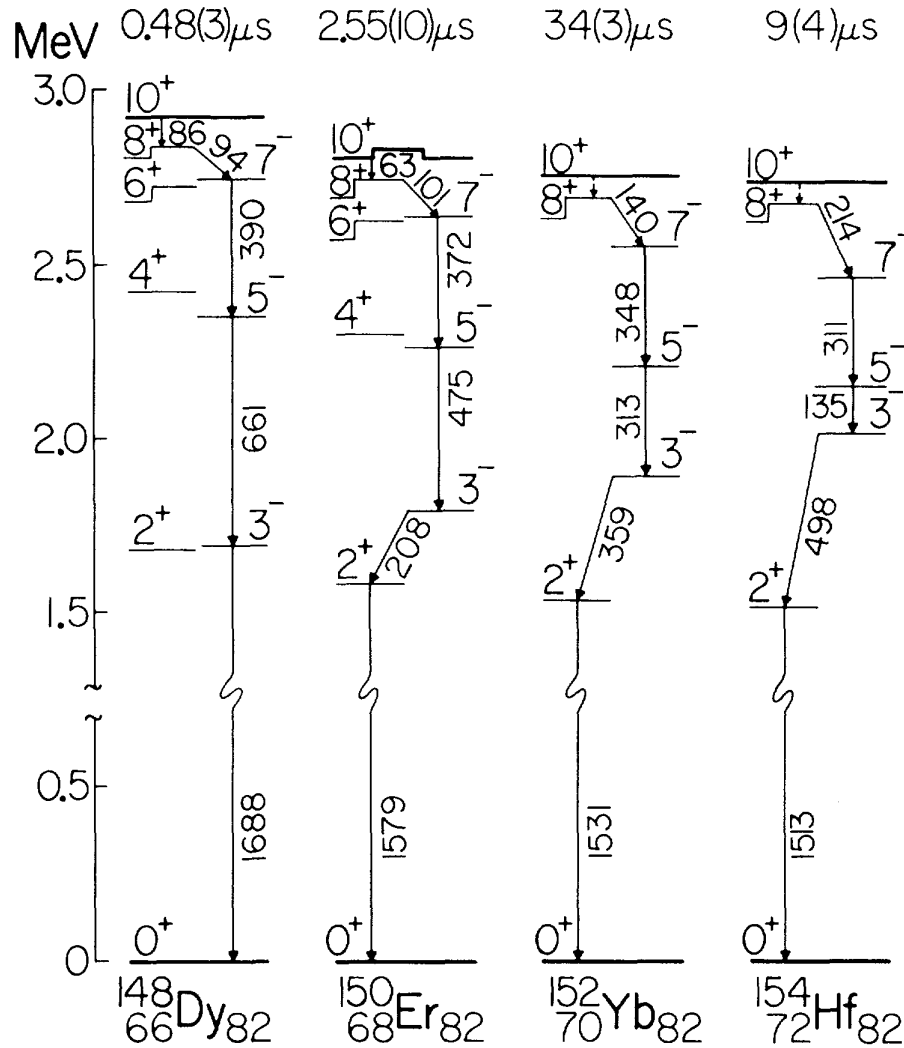Figure 5.1: Energy systematics of N = 82 isotones showing the level scheme below the isomeric 10^+ state [76].

flight methods using the multiwire proportional counters as shown in Fig. 5.2. Gamma rays emitted at the focal plane were detected by a Ge array comprising three HPGe clover detectors and the GREAT planar detector.

All detector signals were passed to the total data readout (TDR) acquisition
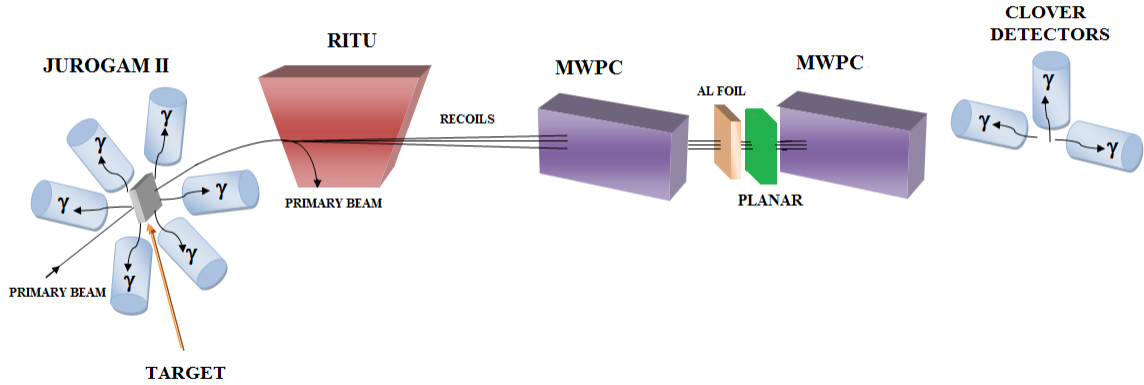
Figure 5.2: Experimental apparatus including the JUROGAM II, the RITU separator and modified focal plane detection system. The modified focal plane includes two MWPC for time of flight measurements, Al stopper foil, three HPGe Clovers and a planar detector.

system [31] where they were time stamped with a precision of 10ns to allow accurate timing correlations between γ rays detected at the target position, recoil implants at the focal plane and their subsequent radioactive decays. These trigger-less data were sorted into γ-ray spectra and γ-γ matrices using GRAIN [15] and analysed with the RADWARE software packages [63].

5.4 Results

5.4.1 Gamma-ray singles measurements

Gamma-ray cascades above isomeric states are emitted and detected promptly at the target position using Jurogam II while the γ rays de-exciting the isomeric state are delayed sufficiently to decay at the focal plane and are detected using the clover and planar detectors. Figure 5.3 shows γ-ray spectra obtained in the present work. Figure 5.3(a) shows γ-ray transitions detected at the focal plane with HPGe detectors. The γ-ray transitions identified previously as belonging to the decay path from the 10^+ $t_{1/2}$=30(1) μs isomer are shown in Fig. 5.3(a). This spectrum was generated by correlations of all γ rays detected in the focal plane Ge array detected with a recoil signal in the second (downstream) multiwire proportional counter. The correlation time was limited to the interval 8 μs to 90 μs in order to eliminate background correlations with short-lived decay products such as ^{152}Tm and ^{153}Yb, which are strong reaction exit channels in these data.

Figure. 5.3(b) shows γ-ray transitions detected at the target position by the JUROGAM II spectrometer and correlated with the 1531 keV ($2^+ \rightarrow 0^+$) isomer-delayed transition detected in the focal plane Ge detectors. The correlation time was limited to a γ-ray detection within the 8 μs to 90 μs range following a recoil event defined by time-of-flight and energy loss signals in the dual MWPC apparatus. These γ rays are assigned as transitions that feed the 10^+ isomeric state in ^{152}Yb.
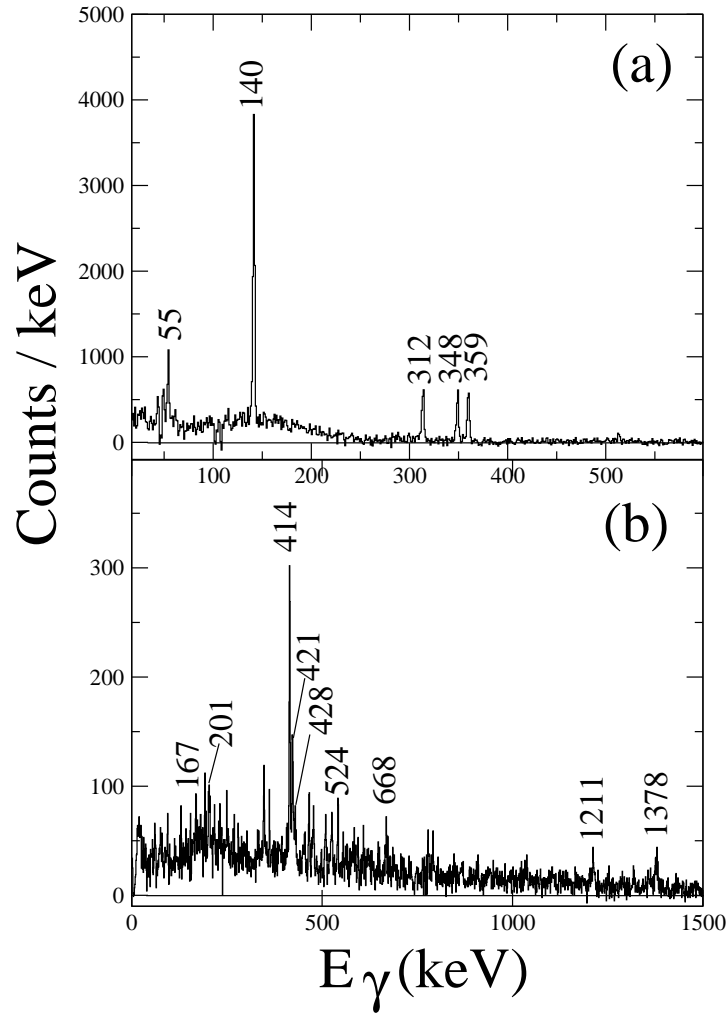
Figure 5.3: (a) Gamma rays detected at the focal plane by HPGe detectors and correlated with recoil events defined by the dual MWPC system. Correlations between the second MWPC and the Ge detectors were limited to 8 μs to 90 μs. (b) Gamma rays detected at the target position and correlated with recoil implantations followed by the 1531 keV $2^+ \rightarrow 0^+$ γ-ray transition in ^{152}Yb. The recoil-γ ray correlation time was limited to 8 μs to 90 μs.

5.4.2 Gamma-ray coincidence measurements

Coincidence spectra are obtained by unfolding the isomer-decay correlated data into two dimensional or three dimensional matrices. The ordering of excited states in ^{152}Yb was obtained from γ-γ coincidences correlated with the delayed 1531 keV using the conditions stated above. Typical isomer-tagged coincidence spectra are shown in Fig. 5.4 and Fig. 5.5. The coincidence analysis indicates that the γ rays are arranged in two distinct cascades. The first sequence involves the 1211 keV, 414 keV and 540 keV transitions. The other cascade involves the 1378 keV, 414 keV, 524 keV and 201 keV γ rays. It is apparent from Fig 5.4(b) that the 414 keV transition is in coincidence with the intense transitions in both cascades. The possibility that the 414 keV γ ray is an energy doublet was explored in relative intensity measurements using isomer-decay tagged singles and coincidence γ-ray spectra. If the ratio of the intensities measured from singles spectra of a two γ-rays are higher than the ratio of the intensities of the same γ- rays obtained from spectra gating on a particular γ-ray with addition of error, means a double γ-ray was found.

Relative intensities of the 414 keV and 201 keV γ rays were obtained from singles (I_s) and coincidence (I_g) spectra and the ratio of intensities were compared. From the two ratios it was observed that when gating on 1378 keV transition the ratio of the intensities of 414 keV and 201 keV had a lower value 1.3±0.4 than the ratio of the same γ rays measured from the singles spectrum 2.8±0.8. Thus the 414 keV γ ray is deduced to be a non-coincident energy doublet.

Angular distribution were performed in order to obtain information about the
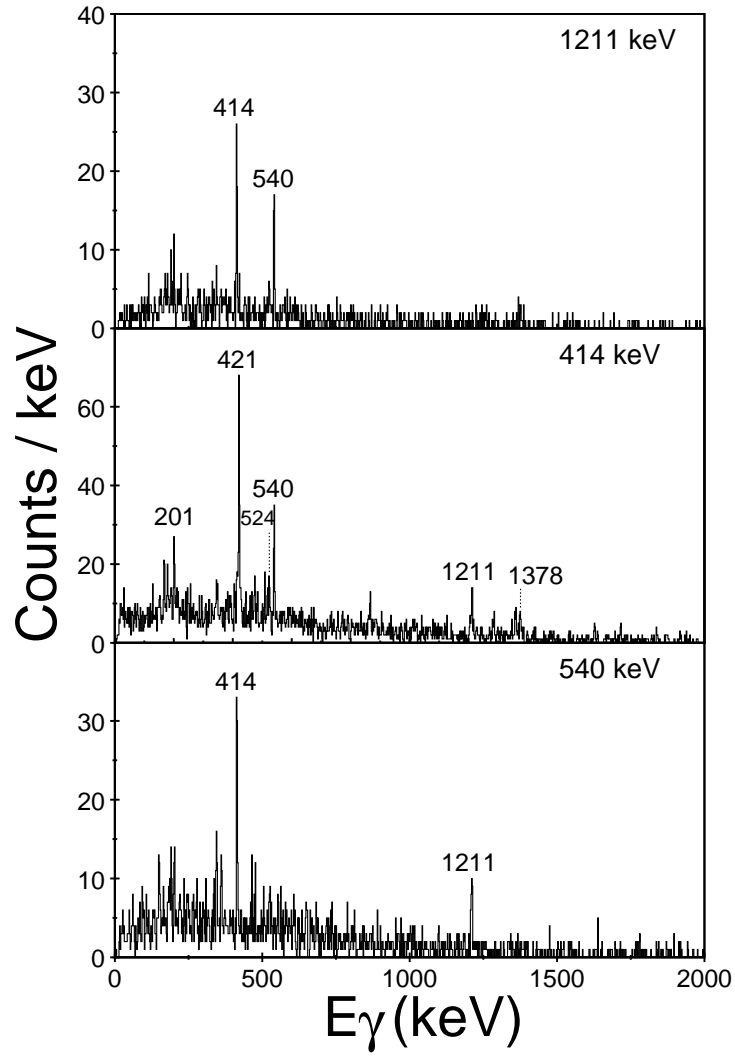
Figure 5.4: Gamma-rays coincidence detected at the target position and correlated with recoil implantations followed by the 1531 keV $2^+ \rightarrow 0^+$ γ-ray transition in ^{152}Yb. The recoil-γ ray correlation time was limited to 8 μs to 90 μs. (a) Gamma-ray coincidences with the 1211 keV transition. (b) Gamma-ray coincidences with the 414 keV transition(s). (c) Gamma-ray coincidences with the 540 keV transition.

Figure 5.5: Gamma-ray coincidences detected at the target position and correlated with recoil implantations followed by the 1531 keV $2^+ \rightarrow 0^+$ γ-ray transition in ^{152}Yb. The recoil-γ ray correlation time was limited to 8 μs to 90 μs. (a) Gamma-ray coincidences with the 1378 keV transition. (b) Gamma-ray coincidences with the 201 keV transition. (c) Gamma-ray coincidences with the 524 keV transition.
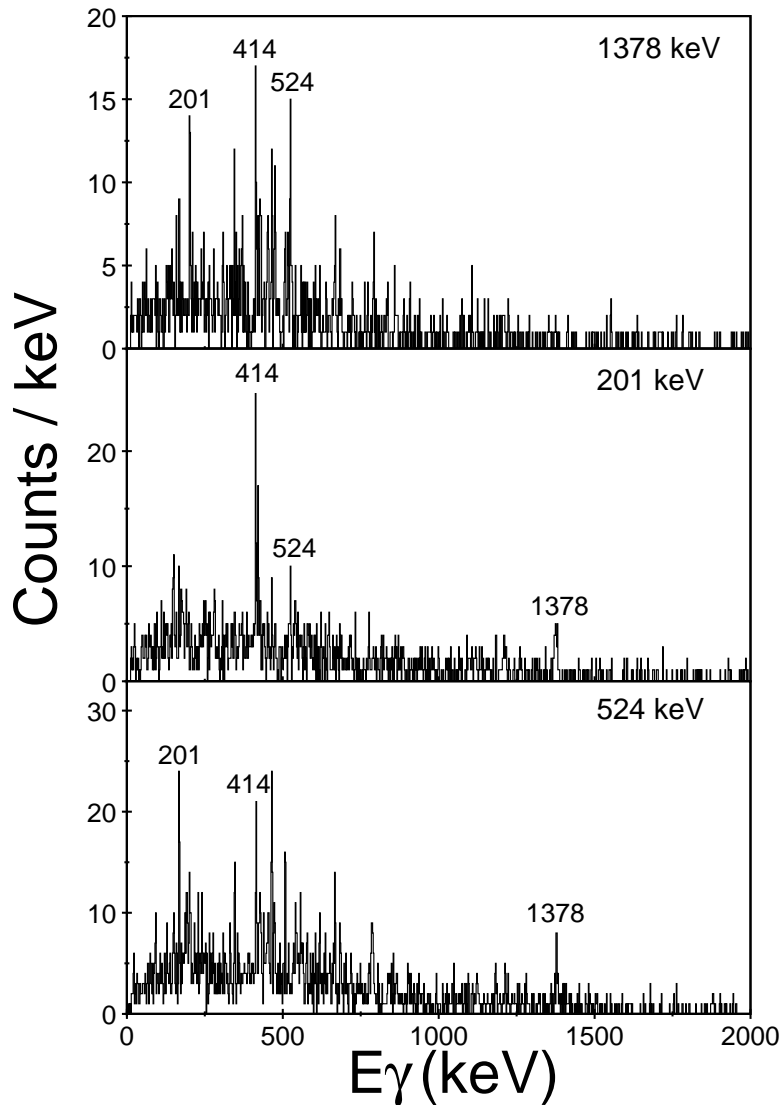
γ-ray multipolarities. The intensities of the γ-rays were calculated as the ratio of the γ-rays intensities detected at angle 157° and 105° relative to the beam direction according to the relation,

$$R = \frac{I(\theta = 157°, allrings)}{I(\theta = 105°, allrings).} \qquad (5.1)$$

To obtain the ratio of the intensities of the γ-rays at particular angles a gate on the self coincident doublet 414 keV was performed. Figure 5.6 shows the measured angular intensity ratios $I_\gamma(157°)/I_\gamma(105°)$ for γ rays assigned to ^{152}Yb. The ratios are benchmarked with measurements obtained for the neutron-deficient ^{153}Tm nucleus [67] (Table 5.2). In the odd nucleus ^{153}Tm the 347 keV transition feeding the $19/2^-$ level has a quadrupole character while the 360 keV has an E2/M1 dipole-quadrupole character. The multipolarity assignments of the $\gamma-$-rays of the ^{153}Tm nucleus were obtained as discussed above by gate on the 648 keV. The 1378 keV with an angular intensity ratio of 0.7 ± 0.2 is assigned a dipole character and is assigned to decay from an 11^- state. This odd spin negative-parity state is analogous to the 11^- states in the other $N = 82$ isotones and is in good agreement with systematics, see Fig. 5.8. The 1378 keV shows a dipole character as the 776 keV in the ^{153}Tm nucleus. The 1211 keV and 540 keV transitions in the parallel cascade are assigned to be electric quadrupoles and form an even-spin positive-parity sequence. The transitions 524 keV and 201 keV yield angular intensity ratios of 0.8 ± 0.1 and 0.8 ± 0.1, respectively and are assigned as dipoles. The three transitions 347 keV, 906 keV and 790 keV have an angular distribution ratio ≥ 1 which is characteristic of a quadrupole multipole similar to the transition of the present work at 540 keV and 1211 keV. The level scheme deduced for
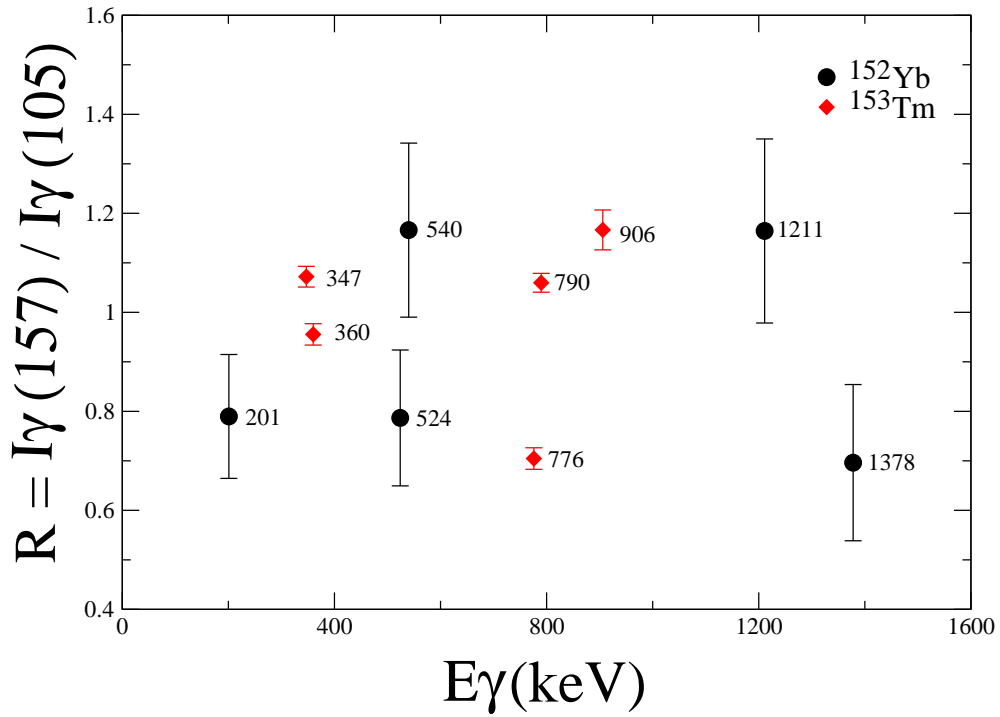
Figure 5.6: The ratio of the intensities measured at 157° and 105° for the nucleus of interest and the strongest channel produced during the fusion evaporation reaction [153]Tm.

[152]Yb is displayed in Fig. 5.7. The relative intensities and correlation measurements are listed in Table 5.1.

Figure 5.7: The level scheme of the ^{152}Yb is presented. The transition energies are given in keV and their relative intensities are proportional to the widths of the arrows.

Table 5.1: Energy, intensities, angular distribution ratios and assignments of the γ rays transitions of ^{152}Yb obtained from tagged singles γ ray spectra.

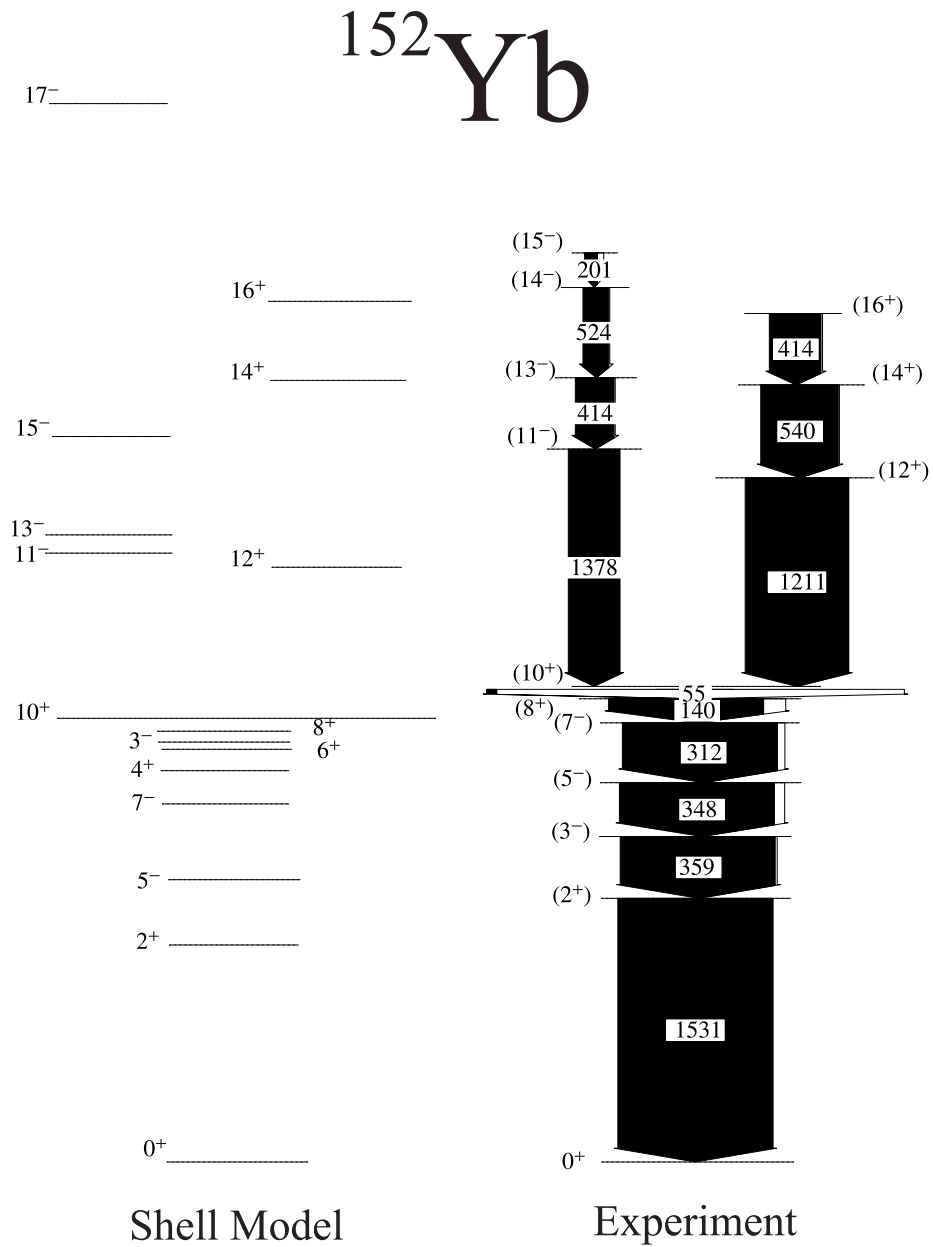| Eγ (keV)	Iγ(%)	R	I$^\pi_{initial} \to$ I$^\pi_{final}$
167	48.5 ± 0.1		
201	36.4 ± 0.1	0.8±0.1	$15^- \to 14^-$
414	100.0 ± 0.0		
421	82.9 ± 0.0		
428	62.6 ± 0.1		
451	27.9 ± 0.2		
465	51.2 ± 0.0		
474	81.7 ± 0.1		
524	62.3 ± 0.1	0.8± 0.1	$14^- \to 13^-$
540	64.7 ± 0.0	1.2± 0.2	$14^+ \to 12^+$
668	55.9 ± 0.2		
1211	36.3 ± 0.1	1.2± 0.2	$12^+ \to 10^+$
1378	49.6 ± 0.1	0.7± 0.2	$11^- \to 10^+$

5.5 Discussion

The newly discovered excited states above the 10^+ isomer in ^{152}Yb are likely to be based on quasiproton excitations since the $N = 82$ shell gap is robust against core excitations at low energies. Indeed spectroscopic studies of the high-spin states in the

Table 5.2: Energy, angular distribution ratio and assignments of the γ rays transitions of ^{153}Tm obtained from γ ray spectrum tagging on 648 keV.

Eγ (keV)	R	I$^\pi_{initial} \to$ I$^\pi_{final}$
347	1.07 ± 0.02	$23/2^- \to 19/2^-$
360	0.96 ± 0.02	$27/2^- \to 25/2^-$
776	0.71 ± 0.02	$29/2^+ \to 27/2^-$
790	1.06 ± 0.02	$15/2^- \to 11/2^-$
906	1.17 ± 0.04	$35/2^+ \to 31/2^+$

heavier $N = 82$ isotones provide an excellent opportunity to establish the variation of high-spin states as a function of solely proton number.

At first glance the structure of the new excited states in ^{152}Yb is similar to the lower mass even-Z isotone ^{150}Er. The positive-parity even-spin cascade in ^{150}Er is generated by $(\pi h_{11/2})^n$ excitations. A maximum spin of $16\hbar$ can be achieved with four protons in the $h_{11/2}$ subshell. The heavier isotone ^{152}Yb has six protons in the $h_{11/2}$ subshell and can generate a spin of $18\hbar$ for the maximally aligned $(\pi h_{11/2})^6$ configuration. This positive-parity sequence comprises the 1211 keV, 540 keV and 414 keV transitions and is likely to be based on a partially aligned $(\pi h_{11/2})^6$ multiplet.

The lowest odd-spin negative-parity state above the 10^+ isomer in ^{152}Yb is an 11^- state. In the lighter $N = 82$ isotones the negative-parity sequences are favoured above and below the 10^+ isomer and are attributed to a $(\pi h_{11/2})^n \otimes 3^-$ phonon configuration. The 13^- and 15^- states have also been observed in the lighter isotones and are inter-

preted as being the lowest energy members of the $(\pi h_{11/2})^{n-1} s_{1/2}$ and $(\pi h_{11/2})^{n-1} d_{3/2}$ multiplets. The maximally aligned negative-parity states based on these configurations could not be established in the present work. The configuration assignments and ordering of excited states above the isomer are reproduced by NuShell [77] truncated shell model calculations, which are compared with the deduced level scheme in Fig. 5.7. The shell-model calculation is performed using the ^{132}Sn (Z = 50, N = 82) core and is truncate by putting 8 protons in $g_{7/2}$ and maximum number of 6 protons in $d_{5/2}$. Levels were calculated for different nucleon configurations, including protons in the $d_{3/2}$, $s_{1/2}$ and $h_{11/2}$ orbitals. The levels selected to be put in the experimental level scheme were the lowest of a given spin. The high-spin excited states above the microsecond isomer in ^{152}Yb show some subtle differences in structure to the lighter isotones. Figure 5.1 highlights the systematic trend of increasing excitation energy with increasing proton number in the negative-parity states. An energy shift of 109 keV in the excitation energy of the 3^- state is observed from ^{146}Gd to ^{148}Dy, which was attributed by Daly [71] to arise from a Pauli interference effect. This interference effect originates from the coupling of the 3^- excitation to the $(h_{11/2})^2_{0^+}$ component of the ^{148}Dy ground state. The heavier even-Z $N = 82$ isotones have multiple 0^+ pairs and should experience an upwards shift that scales with the number of proton pairs. Figure 5.8 shows the variation of the 3^- and 11^- states relative to the ground and isomeric states, respectively as a function of proton number. It can be observed that the addition of protons to the $h_{11/2}$ subshell from ^{148}Dy to ^{154}Hf also results in an increase in the excitation energy of the 11^- states due to the same Pauli interference effect.
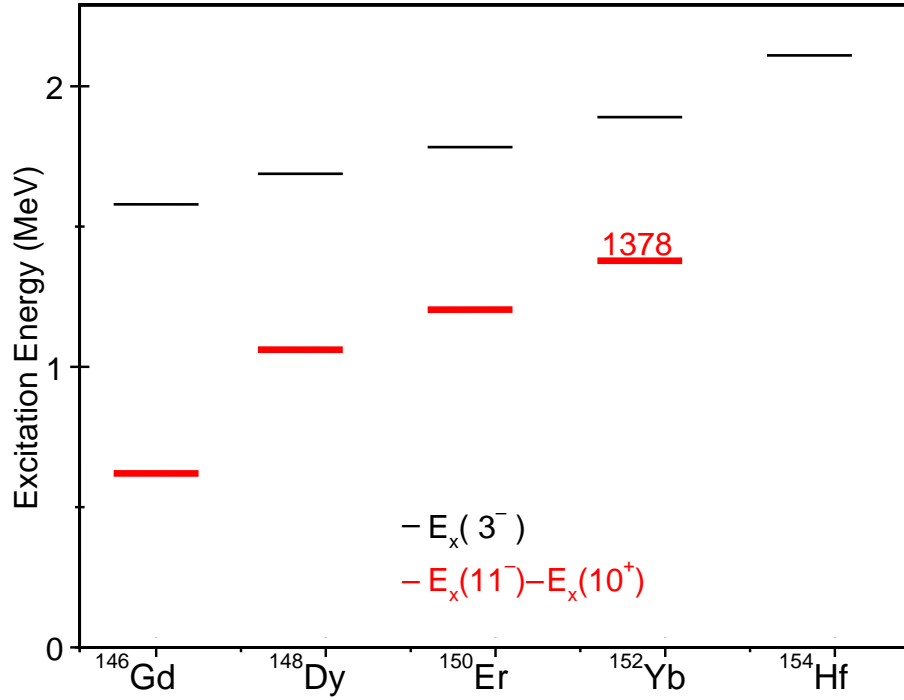
Figure 5.8: Excitation energy of the 3^- state and the energy difference between the J^π $= 11^-$ and 10^+ levels in even-even N $=82$ isotones. Data taken from [78, 71, 73, 75, 76] and from the present work.

The increase of excitation energy in the high-spin negative parity states has consequences for the competing configurations along the yrast line above the 10^+ isomer. Figure 5.9 shows the variation in excitation energy of the 3^- octupole and 2^+ states in even-even $N = 82$ isotones. The figure shows that the 3^- octupole configuration shows a parabolic trend in excitation energy as a function of proton number and reaches a minimum at the $Z = 64$ closed shell. The 2^+ state reaches a maximum value at the $Z = 64$ shell gap and gradually falls towards higher proton
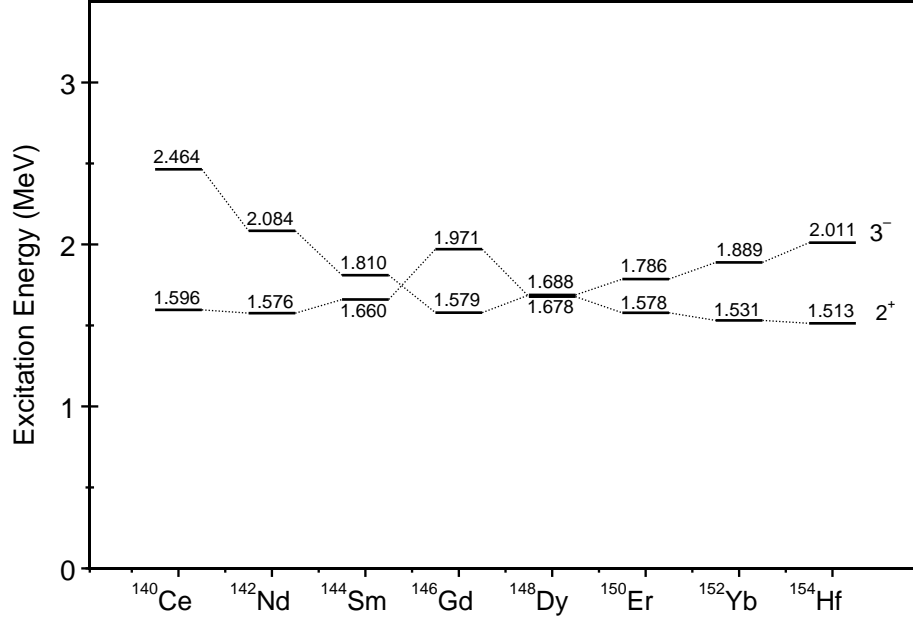
Figure 5.9: The variation in excitation energy of the 3^- octupole and 2^+ states in even-even $N = 82$ isotones [78, 71, 73, 75, 76].

numbers. As a consequence of these trends, the positive-parity $(\pi h_{11/2})^n$ configuration becomes the yrast configuration in ^{152}Yb. Thus ^{152}Yb is the first heavy $N = 82$ isotone in which the 12^+, 14^+ and 16^+ are the yrast configuration above the 10^+ isomer.

5.6   Summary

Gamma rays emitted from the excited states in the semi-magic nucleus ^{152}Yb have been identified using the recoil isomer tagging technique. The level scheme above

the isomeric 10^+ state was established for first time. The configuration assignments have been interpreted in term of OXBASH truncated shell model calculations and compared with the deduced level scheme. Angular distribution were performed in order to obtain information about the γ rays multipolarities.

Chapter 6

Conclusions

The nuclei investigated in this thesis ^{158}W (N = 84) and the semi-magic nucleus ^{152}Yb (N = 82) were produced by performing two experiments utilising the JUROGAM spectrometer, RITU separator and GREAT spectrometer at the University of Jyväskylä. These nuclei have few valence nucleons outside of the N = 82, Z = 82 closed shells and display behaviour that is sensitive to the position of the occupied single-particle orbitals. The ^{158}W and ^{152}Yb nuclei have proved difficult to study due to the relatively low cross sections. Indeed due to the low population of these nuclei, with fusion-evaporation reactions, in-beam studies are only possible using selective techniques.

The N = 84 isotones with Z $\geq$ 64 are spherical and close to the proton drip line. The N = 84 isotones are ideal for studying the neutrons in $f_{7/2}$ and $h_{9/2}$ orbitals as well as the interactions between the neutrons and the protons in the $h_{11/2}$ orbital. The level scheme of the ^{158}W (N = 84) nucleus was obtained for the first time. The

configuration of the 2^+, 4^+ and 6^+ states is $(\nu f_{7/2})^2$ and the configuration of the isomeric 8^+ state is $\nu f_{7/2} h_{9/2}$. The low spin states up to 6^+ in the even-even isotones are generated through successive alignment of valence $f_{7/2}$ neutrons. An attractive interaction between the $h_{11/2}$ protons and $h_{9/2}$ neutrons lowers the excitation energy of the 8^+ state with each pairwise addition of protons. In ^{158}W lowering the energy of the $h_{9/2}$ leads to seniority inversion along the yrast line and the formation of an yrast trap. The lowering of the 8^+ state of configuration $\nu f_{7/2} \, otimes \nu h_{9/2}$ below the 6^+ state $(\nu f_{7/2}^2)$ results in the presence of an 8^+ isomer. The excited states above the 8^+ isomers are interpreted in terms of $(f_{7/2} h_{9/2})$ excitations.

The study of the N $= 82$ isotones reveal an understanding to the proton excitations. The interest in semi-magic nuclei at N $= 82$ started with the discovery of ^{146}Gd as a double magic nucleus. In the semi-magic ^{152}Yb nucleus the level scheme was extended above the isomeric 10^+ state. The $J^\pi = 10^+$ isomeric state have been attributed to the full alignment of two $h_{11/2}$ protons i.e. seniority $\nu = 2$. The excited states of spin $\leq 18\hbar$ are observed in ^{152}Yb by the alignment of $\pi h_{11/2}$ pairs. In the semi-magic nucleus ^{152}Yb the yrast line continues above the isomeric 10^+ state of configuration $(\pi h_{11/2})^2$ by coupling to the octupole excitation. The increasing energy of the octupole excitation as a function of Z for even-even N $= 82$ isotones has been attributed to the Pauli interference effect arising from the coupling of the 3^- excitation and the $\pi(h_{11/2})_{0+}^n$ component of the ground state. Therefore, as the occupation of the $h_{11/2}$ orbital increases so does the interference. A consequence of this effect is that the positive-parity even spin configurations are yrast above 10^+ state in the ^{152}Yb.

References

[1] http://www.nndc.bnl.

[2] http://www.jyu.fi/fysiikka/en/research/accelerator.

[3] E. S. Paul, Postgraduate lecture notes, University of Liverpool, 2012.

[4] M. G. Mayer, Science **145**, 999 (1964).

[5] M. G. Mayer, Physical Review **78**, 16 (1950).

[6] K. S. Krane, *Introductory Nuclear Physics* (John Wiley & Sons, 1988).

[7] K. Siegbahn, *Alpha, Beta and Gamma-Ray Spectroscopy, Volume 2* (North-Holland Publishing Company, Amsterdam, 1968).

[8] K. Siegbahn, *Alpha, Beta and Gamma-Ray Spectroscopy, Volume 1* (North-Holland Publishing Company, Amsterdam, 1968).

[9] G. Gamow, Zeitschrift für Physik **51**, 204 (1928).

[10] H. Ejiri and M. J. A. de Voigt, *Gamma-ray and electron spectroscopy in nuclear physics* (Oxford University Press, 1989).

[11] A. deShalit and I. Talmi, *Nuclear shell theory* (Academic Press Inc. (London), 1963).

[12] K. S. Krane, Atomic Data and Nuclear Data Tables **16**, 383 (1975).

[13] P. M. Walker and G. D. Dracoulis, Hyperfine Interactions **135**, 83 (2001).

[14] P. M. Walker and G. D. Dracoulis, Nature **399**, 35 (1999).

[15] P. Rahkila, Nuclear Instruments and Methods in Physics Research Section A **595**, 637 (2008).

[16] P. H. Regan, *Experimental Nuclear Techniques, Postgraduate Lecture Course Notes* (University of Surrey, Unpublished., 2003).

[17] R. S. Simon *et al.*, Zeitschrift für Physik A **325**, 197 (1986).

[18] E. S. Paul *et al.*, Physical Review C **51**, 78 (1995).

[19] J. Eberth and J. Simpson, Progress in Particle and Nuclear Physics **60**, 283 (2008).

[20] G. F. Knoll, *Radiation Detection and Measurement*, Third ed. (John Wiley & Sons, 2000).

[21] http://www.jyu.fi/fysiikka/en/research/accelerator/nucspec_old/gamma/jurogam/.

[22] Jyfl accelerator news, University of Jyvaskyla, Finland, 2008.

[23] P. J. Nolan, F. A. Beck, and D. B. Fossan, Annual Review of Nuclear and Particle Science **44**, 561 (1994).

[24] C. W. Beausang *et al.*, Nuclear Instruments and Methods in Physics Research Section A: Accelerators, Spectrometers, Detectors and Associated Equipment **313**, 37 (1992).

[25] P. J. Nolan, Nuclear Physics A **520**, 657c (1990).

[26] https://www.jyu.fi/fysiikka/en/research/accelerator/nucspec/jurogam/photos/drawings/.

[27] M. Leino *et al.*, Nuclear Instruments and Methods in Physics Research Section B **99**, 653 (1995).

[28] N. Bohr, Physical Review **58**, 654 (1940).

[29] A. Ghiorso *et al.*, Nuclear Instruments and Methods in Physics Research Section A: Accelerators, Spectrometers, Detectors and Associated Equipment **269** (1987).

[30] R. D. Page *et al.*, Nuclear Instruments and Methods in Physics Research Section B **204**, 634 (2003).

[31] I. H. Lazarus *et al.*, IEEE Transactions on Nuclear Science **48**, 567 (2001).

[32] A. Keenan *et al.*, Physical Review C **63** (2001).

[33] S. L. King *et al.*, Physical Review C **62**, 067301 (2000).

[34] S. L. King *et al.*, Physical Letters B **443**, 82 (1998).

[35] D. T. Joss *et al.*, Physical Review C **70**, 6 (2004).

[36] D. T. Joss *et al.*, Physical Review C **74**, 1 (2006).

[37] D. Seweryniak *et al.*, Physical Review C **71**, 1 (2005).

[38] B. Cederwall *et al.*, Physics Letters B **443**, 69 (1998).

[39] J. Thomson, *Yrast states in the neutron-deficient isobars* ^{163}W *and* ^{163}Ta, PhD thesis, University of Liverpool, 2009.

[40] J. Simpson *et al.*, Journal of Physics G **17**, 511 (1991).

[41] J. Simpson *et al.*, Journal of Physics G **18**, 1207 (1992).

[42] K. Theine *et al.*, Nuclear Physics A **548**, 71 (1992).

[43] J. Recht *et al.*, Physics Letters B **122**, 207 (1983).

[44] G. D. Dracoulis, P. M. Walker, and A. Johnston, Journal of Physics G **4**, 713 (1978).

[45] G. D. Dracoulis and P. M. Walker, Nuclear Physics A **330**, 186 (1979).

[46] D. T. Joss *et al.*, Nuclear Physics A **689**, 631 (2001).

[47] G. D. Dracoulis *et al.*, Nuclear Physics A **486**, 414 (1988).

[48] J. L. Durell, G. D. Dracoulis, C. Fahlander, and A. P. Byrne, Physics Letters B **115**, 366 (1982).

[49] G. D. Dracoulis, C. Fahlander, and M. P. Fewell, Nuclear Physics A **383**, 119 (1982).

[50] K. Y. Ding *et al.*, Physical Review C **62**, 1 (2000).

[51] H. Hübel *et al.*, Zeitschrift für Physik A **329**, 289 (1988).

[52] K. P. Blume *et al.*, Nuclear Physics A **464**, 445 (1987).

[53] R. Chapman *et al.*, Physical Review Letters **51**, 2265 (1983).

[54] J. C. Lisle, J. D. Garrett, G. B. Hagemann, B. Herskind, and S. Ogaza, Nuclear Physics **A366**, 281 (1981).

[55] E. S. Paul *et al.*, Journal of Physics G **11**, L53 (1985).

[56] P. M. Walker *et al.*, Physics Letters B **168**, 326 (1986).

[57] T. L. Khoo, F. M. Bernthal, R. G. H. Robertson, and R. A. Warner, Physical Review Letters **37**, 823 (1976).

[58] J. Thomson *et al.*, in preparation .

[59] G. D. Dracoulis *et al.*, Proceedings of the International conference of Nuclear Structure at High Angular Momentum **2**, 92 (1992).

[60] S. Hofmann *et al.*, Zeitschrift für Physik A **333**, 107 (1989).

[61] R. D. Page *et al.*, Physical Review C **53**, 660 (1996).

[62] C. W. Beausang and J. Simpson, Journal of Physics G **22**, 527 (1996).

[63] D. C. Radford, Nuclear Instruments and Methods in Physics Research Section A **361**, 297 (1995).

[64] B. Brown *et al.*, MSU-NSCL rep. num. (2004) 1289., 2004.

[65] C. T. Zhang *et al.*, Physical Review C **54**, R1 (1996).

[66] J. H. McNeill *et al.*, Zeitschrift für Physik A **344**, 369 (1993).

[67] C. T. Zhang *et al.*, Zeitschrift für Physik A **348**, 249 (1994).

[68] K. Y. Ding *et al.*, Physical Review C **64**, 1 (2001).

[69] C. T. Zhang *et al.*, Zeitschrift für Physik A **345**, 327 (1993), 10.1007/BF01280841.

[70] A. Kuhnert *et al.*, Physical Review C **46**, 484 (1992).

[71] P. J. Daly *et al.*, Zeitschrift für Physik A **298**, 173 (1980).

[72] J. Wilson *et al.*, Zeitschrift für Physik A **296**, 185 (1980).

[73] Y. H. Chung *et al.*, Physical Review C **29**, 2153 (1984).

[74] E. Nolte *et al.*, Zeitschrift für Physik A **306**, 211 (1982).

[75] D. T. Nisius *et al.*, Physical Review C **52**, 1355 (1995).

[76] J. H. McNeill *et al.*, Physical Review Letters **63**, 860 (1989).

[77] B. A. Brown and W. D. M. Rae, Nushell@msu, MSU-NSCL report, 2004.

[78] P. Kleinheinz *et al.*, Zeitschrift für Physik A **290**, 279 (1979).